Deformation Mode and Strain Path Dependence of Martensite Phase Transformation in a Medium Manganese TRIP Steel

Wei Wu, Yu-Wei Wang, Panagiotis Makrygiannis, Feng Zhu, Grant A. Thomas, Louis G. Hector, Xiaohua Hu, Xin Sun, Yang Ren

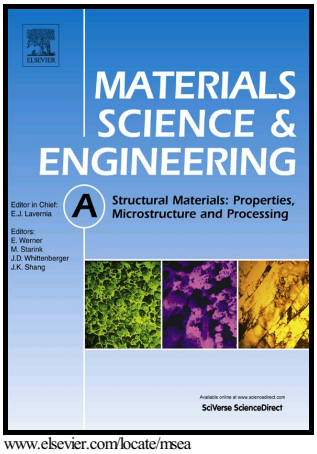

www.elsevier.com/locate/msea

PII: S0921-5093(17)31458-2
DOI: https://doi.org/10.1016/j.msea.2017.11.008
Reference: MSA35723

To appear in: *Materials Science & Engineering A*

Received date: 7 September 2017
Revised date: 2 November 2017
Accepted date: 3 November 2017

Cite this article as: Wei Wu, Yu-Wei Wang, Panagiotis Makrygiannis, Feng Zhu, Grant A. Thomas, Louis G. Hector, Xiaohua Hu, Xin Sun and Yang Ren, Deformation Mode and Strain Path Dependence of Martensite Phase Transformation in a Medium Manganese TRIP Steel, *Materials Science & Engineering A,* https://doi.org/10.1016/j.msea.2017.11.008

Deformation Mode and Strain Path Dependence of Martensite Phase Transformation in a Medium Manganese TRIP Steel

Wei Wu[1], Yu-Wei Wang[1*], Panagiotis Makrygiannis[1], Feng Zhu[1], Grant A. Thomas[2], Louis G. Hector, Jr.[3*], Xiaohua Hu[4], Xin Sun[5], Yang Ren[6]

[1]AK Steel Research and Innovation, AK Steel Corporation, Dearborn, MI 48120, USA
[2]AK Steel Research and Innovation, AK Steel Corporation, Middletown, OH 45005, USA
[3]GM R&D Center, General Motors Corporation, Warren, MI 48092, USA
[4]Pacific Northwest National Laboratory, P.O. Box 999, Richland, WA 99352, USA
[5]Oak Ridge National Laboratory, Oak Ridge, TN, 37930, USA
[6]X-ray Science Division, Argonne National Laboratory, Argonne, IL 60439, USA

*Corresponding authors
Yu-Wei Wang, Ph.D.
Section Manager
Research and Innovation
Advanced Engineering
AK Steel Corporation
14661 Rotunda Dr.
Dearborn
MI 48120, USA
Office: +1-313-317-1301
E-mail: Yu-Wei.Wang@aksteel.com

Louis G. Hector, Jr, Ph.D.
Technical Fellow
GM R&D Center
General Motors Corporation
30500 Mound Road
Warren
MI 48090, USA
Office: +1-586-651-2628
E-mail: Louis.Hector@gm.com

ABSTRACT

The martensite phase transformation dependence upon deformation modes and strain paths in a medium manganese (10 *wt.*%) TRIP steel stamped into a T-shape panel was quantified through combination of a 3D digital image correlation and synchrotron X-ray diffraction. The T-shape emulates a portion of a common anti-intrusion component. The stamping speed was kept intentionally slow (1 mm/s) so as to avoid excessive heat generation. The steel, which belongs to the third generation advanced high strength steel (3GAHSS) family, was chosen for two reasons: (1) it is two-phase, i.e. austenite and ferrite, with martensite resulting from deformation-induced phase transformation; (2) the 66 *vol.*% initial retained austenite volume fraction (RAVF) enabled a thorough examination of the martensite phase transformation at large deformation levels without exhaustion. Strain fields were coupled with measured RAVF values of small specimens extracted from specific locations on a formed T-shape panel. This enabled an exploration of the effects of linear, bilinear and non-linear strain paths as well as deformation modes such as tension, plane strain, biaxial tension and equibiaxial tension. Results suggest a significant martensite phase transformation dependence on deformation mode and strain path in the absence of fracture and when martensite phase transformation is unaffected by heat generated during forming. In general, the uniaxial and biaxial tension deformation modes facilitate the martensite phase transformation, while the smallest amount of martensite phase transformation occurs under plane strain. Some discussion as to further application of the experimental methods detailed in this study to other 3GAHSS and the effects of fracture on martensite phase transformation is provided.

Keywords: Deformation modes; Martensite phase transformation; Non-linear strain path

1. Introduction

The third generation advanced high strength steels (3GAHSS) offer combinations of strength and ductility that are potentially favorable for automotive component forming. Their macroscopic-scale mechanical properties, as represented by an advanced high strength steel (AHSS) tensile strength-ductility chart [1], are typically intermediate to those of the high strength/lower ductility first generation advanced high strength steels (1GAHSS), and the high strength/high ductility second generation advanced high strength steels (2GAHSS) [2]. As-received 3GAHSS microstructures are multiphase and may consist of combinations of body-centered cubic (BCC) ferrite, face-centered cubic (FCC) austenite, and body-centered tetragonal (BCT) martensite phases produced from sophisticated alloying and heat treatment schemes. The ferrite (α) phase controls ductility, while strength is enhanced by martensite (α') as well as bainitic ferrite. A common deformation mechanism in many 3GAHSS is the transformation induced plasticity (TRIP) [3] effect, i.e., the diffusionless shear transformation of metastable retained austenite (γ or RA) to new martensite (also BCT) with plastic straining [3]. The combination of phases and the martensitic transformation of austenite enhances the work hardening rate and improves strength and ductility thereby delaying fracture: this is especially favorable for automotive applications. In some cases, the austenite to martensite transformation may occur via an intermediate step through ε-martensite, the non-magnetic, HCP form of martensite, [4]. Subsequent transformation of ε-martensite to α'-martensite at intersections of shear bands has been experimentally confirmed in the literature [5, 6].

The 3GAHSS are also distinct from the first generation (1GAHSS) TRIP steels [1] by virtue of a higher retained austenite (γ or RA) volume fraction (RAVF) and Mn content [e.g. 3-12 weight percentage (*wt.*%)]. The 3GAHSS alloying typically differs from that of the low stacking fault twinning induced plasticity (TWIP) steels, which are 2GAHSS, wherein Mn content can range from 15-25 *wt.*% [7, 8] and austenite is stable against transformation. Steels that exhibit both the TRIP and TWIP effects with 15-25 *wt.*% Mn have also been identified [9, 10]. In addition to the TWIP and TRIP effects, dislocation glide [11] also occurs, with one mechanism predominating over others within a specific temperature range.

Examples of 3GAHSS are Medium Mn (~3-12 *wt.*% Mn) TRIP steels [12], TRIP steels with a bainitic ferrite matrix (TBF steels) [13], and TRIP steels subject to a quenching and partitioning (Q&P) heat treatment (also known as QP steels with ~3 *wt.*% Mn) [14]. Of these materials, the Medium Mn TRIP steels, in which austenite is stabilized through enrichment with Mn, have recently received considerable attention in the literature since they are produced through intercritical annealing in the ferrite–austenite region, a processing route that might be somewhat simpler than Q&P [10, 15], for example. In addition, they provide strengths and ductilities well within the range of 3GAHSS. Therefore, there is still considerable interest in understanding the microstructure evolution during alloy processing and the effect of microstructure on component manufacturing and performance [16-18]. A TBF microstructure results from cooling to just above the martensite start temperature thereby allowing bainitic ferrite to form with C partitioning to the remaining austenite. Although there are different variants of the Q&P process, the essential approach is heating to a temperature above the

austenitization temperature, which can be followed by an immediate quench to a temperature between the martensite start and finish temperatures. Carbon mobility and subsequent carbon enrichment of austenite occurs during a final partitioning step which enhances austenite stability. The size and morphology of austenite is somewhat varied in QP steel. Xiong et al. [19] found that film-like (< 1.0 μm) and blocky (≥ 1.0 μm) austenite in a Fe-0.22C-1.4Si-1.8Mn (*wt.*%) TRIP steel subject to a Q&P heat treatment transformed at different tensile strains. In general, the RAVF decreases with increasing plastic strain and can be measured with a variety of methods including synchrotron X-ray diffraction [20, 21] (or high energy X-ray diffraction, HEXRD), neutron diffraction [22] and additional techniques such as those detailed by Jacques et al. [23].

The mechanical stability of austenite is dependent upon temperature [24] and strain rate [25-27], deformation mode [28-30], strain path [31, 32], chemistry (e.g. carbon concentration), and morphology (e.g. film or blocky) [19]. Previous research reported in the literature has largely focused on measuring retained austenite transformation (e.g. RAVF or RAVF vs. strain) in AHSS almost exclusively for quasi-static, uniaxial tension under different thermal conditions [12, 20, 33-40]. Diffraction techniques have been successfully employed to investigate deformation mechanisms in uniaxial and cyclic loading conditions [41-47]. There are, however, some notable exceptions where austenite transformation under deformation modes other than tension has been explored. For example, Yan et al. [48] measured RAVF vs. effective strain in a 0.21C–1.5Si–1.0Mn TRIP steel subject to three different deformation modes, viz., uniaxial tension, biaxial and plane strain deformation. Martensite phase transformation, measured with an X-ray diffractometer technique using Cr Kα radiation [49], was fastest under plane strain

deformation which the authors concluded was the most favorable deformation mode. Iwamoto et al. [28] employed an X-ray diffractometer with a Mo Kα X-ray source measuring martensite phase transformation in various TRIP steels. For small strains, a significant volume of martensite was noted under compression. However, this changed at higher strains with tension giving the greater volume of martensite. Choi et al. [50] developed a microstructure-based finite element model to investigate deformation and failure of a commercial Fe-0.18C-1.62Si-1.75Mn (*wt.*%) TRIP800 alloy. They predicted the most rapid transformation of austenite to occur under equi-biaxial stretching, while transformation was slowest under shear. Gnäupel-Herold and Creuziger [22] employed neutron diffraction to measure austenite transformation in commercial TRIP590, TRIP700 and TRIP780 steels under uniaxial tension, biaxial and plane strain deformation. With a combined neutron diffraction and digital image correlation (DIC) technique, Jacques et al. [51] reported that faster austenite transformation rates corresponding to higher hardening at smaller strains occurred at stress states between uniaxial and equi-biaxial tension for two TRIP steels.

At present, no attempts to quantify the dependence of local RAVF on deformation and strain path in a stamped, 3GAHSS component could be located in the literature. This data is critical as it is the first step towards quantitatively linking local ductility, strength and fracture mechanism to 3GAHSS component performance under complex loading paths. Such linkages will be required not only for alloy development and material selection but also for the development of mechanism-based material constitutive models for finite element simulations. There are in fact very few studies in the literature that attempt to link RAVF to local properties in a formed (e.g. room temperature stamped)

AHSS component. For example, Kobayashi et al. noted that stretch flangeablity is dependent, in part, on the martensite phase transformation in TRIP steel and the associated relaxation of local stresses [52]. Sugimoto and Srivastava observed that superior impact toughness of TRIP steels is dependent upon RAVF [53]. Lacroix et al. [54] found that tearing resistance of TRIP-assisted steels is improved with higher austenite mechanical stability. In their study of a 0.1C–1.5Si–1.5Mn–0.5Cu TRIP-assisted steel, Lee et al. [55] attempted to connect retained austenite stability and formability and found better formability in specimens with greater austenite stability.

In this paper, RAVF variations with deformation mode and strain path were measured at specific positions around a T-shaped panel stamped from a two-phase medium Mn (10 *wt.*%) TRIP steel with a large (~66%) initial austenite volume fraction. The panel emulates a portion of a common automotive stamping. The positions chosen for measurement were subject to different deformation modes and strain paths as verified with a three-camera DIC technique used to measure the major and minor strains during forming. The forming speed was sufficiently slow so as not to inhibit martensite phase transformation through excessive heat generation thereby enabling measurement of data in the limit of room temperature deformation. This is a critical first step for assessment of material constitutive models for component forming and performance. Following DIC measurement of the formed panel, small specimens were extracted from the specific positions for RAVF measurements using high-energy synchrotron X-ray diffraction at the Advanced Photon Source (APS), Argonne National Laboratory (ANL). Representative results that show the deformation and strain path dependence of RAVF are presented in a plot of major vs. minor strain (or “forming limit diagram space”) with the corresponding

value of local RAVF decrease in the formed panel. The results provided a comprehensive examination of deformation-induced martensite phase transformation under various strain paths, ranging from tension to biaxial.

2. Materials and Experimental Procedures

2.1 Med. Mn (10 *wt.*%) TRIP Steel

A Medium Manganese (Fe-0.15C-10Mn-1.5Al-0.2Si, *wt.*%)) TRIP steel, hereinafter referred to as Med. Mn (10 *wt.*%) TRIP, with mechanical properties within the 3GAHSS family, was developed for this study. No coating was applied to the material. Tensile properties over a range of nominal strain rates are detailed in Appendix A. Processing involved intercritical batch annealing at 600-700 °C for 96 hours. According to Gibbs et al. [12], this facilitates enrichment of retained austenite with both C and Mn. The material was then hot rolled in billet form and then cold rolled into 1500 mm long strips each with a nominal 1.1 mm thickness and 200 mm width. The chemical composition in weight percentage is listed in Table 1. The as-manufactured material contains ~66 % retained austenite by volume fraction with the balance ferrite. The large initial volume fraction was deemed suitable for the present study since focus was on deformation mode and strain path dependence of martensite phase transformation in a 3GAHSS formed panel. Hence, it was unlikely that retained austenite would be completely exhausted at some positions selected for RAVF measurement on the final formed panel. A field emission SEM image of the as-manufactured microstructure is exhibited in Fig. 1 showing the ferrite and austenite phases. The average grain size of the Med. Mn (10 *wt.*%) TRIP was approximately 2 μm.

2.2. Stamping Die Set

The laboratory T-shape stamping die set shown in Fig. 2(a) was designed to generate deformation modes (e.g. biaxial tension, uniaxial tension, and plane strain,) and strain paths (i.e. linear, bi-linear, and non-linear) in a stamped panel for subsequent strain and RAVF measurements at discrete locations. Stamping of a flat Med. Mn (10 *wt.*%) steel blank produced a shell structure with a T-shaped profile having a maximum 25 mm stamping depth. The T-shape geometry mimics a section of generic b-pillar which is a common anti-intrusion component in vehicle body structures. The die set is integrated into an Interlaken S225 hydraulic press, which contains two actuators that enable double action: a blank holder actuator and a stamping actuator. Each actuator has a maximum 350 mm displacement operating within a speed range of 0.01-25 mm/s. For all stampings in the present study, a 1 mm/s actuator speed was used. This speed was sufficiently slow so that martensite phase transformation is not suppressed by the excessive heat generation and strain rate effects can also be avoided (see Appendix A) [56]. The maximum force was 1000 kN for each actuator. No lubricant was applied in the current study during forming.

The T-shape die set includes an upper die, shown in Fig. 2(b), and a lower binder and lower punch, shown in Fig. 2(c). The die cavity depth is adjustable from 17 to 25 mm using shims. A step bead, shown in Fig. 2(c), was added to control material flow as the blank is clamped first between the upper die and the lower binder. Since material along the top of the T-shape, which is flat, accumulates minimal strain during stamping, a center pocket was added to the upper die along with a matching recession in the lower punch, shown in Figs. 2(b) and (c). The center pocket follows a square profile with

rounded corners. Its depth can be adjusted with shims to induce various deformation modes, strain paths, and strain gradients along the center pocket. When the T-shape die is fully closed, the gap between the die cavity and punch is 1.4 mm, which allows the maximum blank thickness of 1.2 mm for testing. After material flow control is established upon application of the binder load, the clamped blank is subsequently formed by the lower punch until a T-shape shell structure results. In multiple tests, the selected stamping parameters were such that no cracking or necking was noted in any of the formed Med. Mn (10 *wt.*%) TRIP steel panels in this study.

2.3 Blank Geometry

T-shaped panels were stamped from the trapezoid blank geometry displayed in Fig. 3(a). The blank thickness in the current study was 1.1 mm. Each blank was cut from strips of the Med. Mn (10 *wt.*%) TRIP steel using wire electrical discharge machining (wEDM). The tapered end of each blank was aligned with the "T" end of the lower punch shown in Fig. 2(c) prior to stamping. Figure 3(b) shows a fully formed T-shaped panel. This adopts the lower punch geometry shown in Fig. 3(b) with a top surface containing the imprint of the center pocket, a flange region along the lower binder, and a vertical wall connecting the two.

2.4 Strain Measurement

A custom three-dimensional (3D) digital image correlation (DIC) system was applied to compute the strain distributions from measured displacement fields of the T-shape panels formed from blanks of Med. Mn (10 wt.%) TRIP steel under incremental

stamping, as shown in Fig. 4(a). The stereoscopic configuration of a three-camera system was attached to the Interlaken press, as shown in Fig. 4(a), which is specifically designed for forming limit and hole expansion measurements (not considered in this study). The resolution of each CCD camera is 2452 x 2056 pixel^2 and each generates an HDF5 data file. Three Allied Vision Stingray CCD cameras, each with a 5 Megapixel resolution and maximum 9 fps framing rate, were positioned such that the field of view in adjacent cameras overlapped to enable imaging of the entire surface of a T-shaped panel. Each used a 50 mm lens. All blanks were cleaned with a combination of acetone and ethyl alcohol. A DIC contrast pattern, consisting of a thin layer of flat white paint evenly applied over a blank surface followed by flat black paint speckles, was then applied to the blank surfaces. A representative contrast pattern is shown in Fig. 3(b). The black droplets were applied randomly, such that the nominal diameter of each droplet did not exceed ~ 25% of the chosen pixel subset size in DIC post-processing of strains. This pattern also enabled suitable control of glare. The three cameras were then calibrated with a standard. Additional details behind the multi-camera DIC technique for strain measurement used in this study are in Refs. [57-59].

Since the T-shape die is a close-die test, strain evolution during forming was measured ex situ under incremental stamping. Here, reference images of the contrast pattern on the blank surface from each of the three cameras were first recorded at a designated location to minimize the rigid movement of the T-shape panel. The forming process was interrupted every 1 mm of forming depth, with the T-shape panel then removed from the die. An image from each of the three cameras was then recorded for strain measurement at the corresponding forming depth on the evolving T-shape shell

structure surface relative to the initial blank with the DIC cameras. This process, which required re-positioning the T-shaped panel in the same designated location as were recorded a few images of the blank surface prior to forming, was continued until the maximum 25 mm forming depth was achieved. A typical loading curve for a Med. Mn (10 *wt.*%) TRIP T-shape panels during incremental forming is shown Fig. 4(b).

Once forming was completed, true major and minor strain distributions on a T-shape panel were parsed in a post-processing step from the collected images using the DANTEC DYNAMICS ISTRA 4D commercial software [60]. The true major and minor strain from DIC measurements are the principal strains in the sheet metal plane. For the DIC data analysis process, an optimal set of parameters was selected, with a pixel subset or facet size of 41 pixels, grid point spacing of 9 pixels, and 3D residuum of 0.4 pixel size, to achieve the quality strain data with limited error bar. A custom computer program was developed to further analyze the image data using Igor Pro software [61]. This enabled calculation of the thickness and effective strain distributions as well as the ratio of minor to major strain distribution for determination of deformation mode. Based on the assumption of constant volume, the thickness strain was calculated from the major and minor principal strains with,

$$\boldsymbol{\varepsilon_3 = -(\varepsilon_1 + \varepsilon_2)} \quad (1)$$

where ε_1, ε_2, and ε_3 are major, minor, and thickness strains, respectively. The DIC measurement technique was validated by comparing the computed thickness strains against thickness strains measured on a Med. Mn (10 *wt.*%) TRIP T-shape panel with an ultrasonic technique [62, 63]. The ultrasonic technique has an accuracy of ~1.0 μm. The

difference of the thickness measurement between the DIC and ultrasonic technique was approximately 1% [64]. In addition, the von Mises effective strain was calculated to quantify the total plastic deformation of a material point.

$$\boldsymbol{\varepsilon_{eff}} = \frac{\sqrt{2}}{3}((\boldsymbol{\varepsilon_1} - \boldsymbol{\varepsilon_2})^2 + (\boldsymbol{\varepsilon_1} - \boldsymbol{\varepsilon_3})^2 + (\boldsymbol{\varepsilon_2} - \boldsymbol{\varepsilon_3})^2)^{1/2} \quad (2)$$

To determine the deformation modes in a T-shape panel, the ratio of minor to major strain, R_1 (= ε_2 / ε_1), was calculated in a customized program using the Igor software at selected forming depths [65]. In general, R_1 = – 0.5 for uniaxial tension; R_1= 0 for plane strain; R_1 = 1 for balanced or equibiaxial tension [66].

2.5 RAVF Measurement

The small specimens for RAVF measurement, each approximately 6 mm x 6 mm, were extracted with wEDM at 24 selected locations around the perimeter of a fully formed Med. Mn (10 *wt.*%) TRIP panel. These locations were chosen to examine as broad a range of deformation modes and strain paths as possible. Some of the specimens had a small degree of curvature but this did not affect RAVF measurement. Specimens were not extracted from the lower portion of the vertical walls that connect with the flange region (noted by lower binder Fig. 2(c)) of a T-shaped stamping. These locations were deemed unsuitable for measurement since the DIC contrast pattern was partially worn off from the walls during stamping thereby precluding strain measurements. The corresponding major and minor strains were extracted from the whole field DIC strain maps in the center of each extracted specimen. In the present paper, only 10 of the 24 extracted specimens were analyzed in detail since these were associated with relevant

deformation modes and strain paths in stamping. The RAVF for each specimen was measured from integrated intensity plots computed from Debye rings generated by the high-energy synchrotron X-ray beamline 11-ID-C at APS, ANL. The 500 μm x 500 μm synchrotron X-ray beam size, with energy and wavelength (λ) of 105 keV and 0.01165 nm, respectively, provided a volumetric measurement since it penetrated the entire specimen thickness. During the 8 sec exposure time, multiple images of the Debye rings from a given specimen were recorded by a PerkinElmer 2D detector and then summed. This gives a significantly improved statistical measurement of the Med. Mn (10 *wt.*%) TRIP microstructure relative to Cu Kα X-ray diffraction (for example) with which penetration depths are limited (e.g. several microns) because of much lower beam energies (8-17 keV). To avoid possible machining effects on microstructure around its edges, each specimen was positioned such that the monochromatic synchrotron X-ray beam impinged its center, corresponding to the DIC strain measurement. This was confirmed with a green laser that followed the same path as the X-ray beam to a specimen surface. Ancillary tests in which the beam location was moved along a circumference at a radius of several millimeters from the center of several specimens revealed no substantive differences in measured RAVF relative to the center location. Hence the centrally-positioned location was deemed representative of the RAVF within the entire specimen. Additional details on the diffraction measurements and extraction of RAVF are in Appendix B.

3. Results and Discussion

The results considered in this section are indicative of those from ancillary tests that were conducted to determine the consistency of the measurement techniques for strain

and RAVF from panel to panel. The analysis of one panel follows, and the corresponding results were determined to be representative of results from 5 T-shape panels produced in this study using the same stamping parameters and instrumentation. No scuffing marks or other features indicative of friction effects were noted on any of the panels. Each Med. Mn (10 *wt.*%) T-shape TRIP steel panel was deformed to the full 25 mm depth allowed by the die set without fracture/splitting.

3.1 Strain Fields from 3D DIC

Determination of locations along the T-shape panel at which RAVF was to be measured was preceded by a careful investigation of strain field development during forming. Figures 5(a)-(i) are DIC-generated contour maps of major, minor, and thickness true strain fields measured during forming of a Med. Mn (10 *wt.*%) TRIP steel panel at 5 mm [Figs. 5(a), (d), and (g)], 15mm [Figs. 5(b), (e), and (h)], and 25 mm [Figs. 5(c), (f), and (i)] depths. The surface of the panel on which strain fields were generated follows that of the punch shape shown in Fig. 2(c). Six locations around the perimeter of the panel are labeled in Figs. 5(c), (f), and (i), viz. i – vi. Locations i and ii represent the left and right (rounded) corners at the bottom (or vertical portion) of the T-shape. Locations, iii and iv denote the lower (rounded) corners of the upper portion (or horizontal portion) of the T-shape, while iv and v denote the upper corners of the upper portion of the T-shape. As stamping progressed from 5 mm to 15 mm, and then to 25 mm, forming depths, peak major and minor strain fields accumulated at these six locations, as expected. Maximum major and minor strains at i – vi achieved values of 0.25 and 0.07, respectively. The flat surface of the panel [denoted by the dark blue surrounded by a lighter outline of the T-shape in Fig. 5(a)] accumulated negligible strains indicating

minimal deformation relative to the rounded corners. When the T-shape panel was stamped to the maximum 25 mm forming depth allowed by the die [see Fig. 2(c)], an impression of the center pocket in the upper die appeared which generated a small strain gradient in that location on the panel, see Figs. 5(c), (f), and (i). Small tensile major and minor strains and compressive thickness strains initially accumulated at locations i – vi at the 5 mm forming depth, as shown in Figs. 5(a), (d), and (g), respectively. At the 15 mm forming depth, strains concentrated at these locations. In addition, tensile minor and compressive thickness strains accumulated in the center pocket region at the 25 mm forming depth. Note that the white spots along the region where the lower radius meets the flange are regions where the DIC contrast pattern was rubbed off during stamping. These regions are especially notable in Figs. 5(b) and (h). This region was removed from consideration in Figs. 5(c), (f), and (i). The compressive minor strains were observed at locations vii and viii in Fig. 5(e) at 15 mm forming depth. The compressive minor strains at location vii and viii became concentrated when the panel was further stamped to 25 mm forming depth in Fig. 5(f).

Effective strain field (ε_{eff}) contour maps at the 5 mm, 15 mm, and 25 mm forming depths are shown in Figs. 6(a)-(c), respectively. Each contour map was computed using DIC-generated strains in Eq. (2). Peak values of the effective strain field appear at all rounded corners, as expected, which are denoted by labels i – vi in Fig. 6(c). This is consistent with the strain fields shown in Fig. 5. Very small effective strains are relatively evenly distributed around the upper radius along the horizontal portion of the Med. Mn (10 *wt.*%) T-shape panel at the 5 mm forming depth in Fig. 6(a). When the forming depth reached 15 mm, the effective strain around the upper radius increased with strain

concentration at locations i – vi in Fig. 6(b). When the T-shape panel was further stamped to the maximum (and final) 25 mm forming depth, severe strain concentration appears at locations i – vi as denoted in Fig. 6(c). Moreover, a non-negligible effective strain concentration appears in the center pocket region in Fig. 6(c).

Deformation mode contours of the T-shape panel calculated as $R_1 = \varepsilon_2 / \varepsilon_1$, where ε_2 and ε_1 are the true minor and major strain fields, respectively, from DIC, are shown in Figs. 6(d)-(f) for forming depths of 5, 15, and 25 mm, respectively. Colors in the key to the right of Fig. 6(f) denotes the range of deformation modes. The values of $R_1 = – 0.5$, 0, and 1 represent uniaxial tension, plane strain, and equibiaxial tension, respectively. For example, Fig. 6(d) shows that at 5 mm forming depth, the locations i – vi underwent plane strain deformation due to pure bending, while material around the upper radius of the horizontal portion of the T-shape panel deformed under a biaxial tension deformation mode (light yellow). Alternatively, material at locations i – vi in Figs. 6(e) and (f) was subject to biaxial tension deformation close to the equibiaxial tension deformation mode as indicated by the red/white contours of R_1. A similar observation holds for material in the curved regions between the upper and lower portions of the T-shape. Meanwhile, locations vii and viii at 15 and 25 mm forming depth deformed under a uniaxial tension deformation mode. Material at the center of the pocket was subject to biaxial tension. At the 25 mm forming depth, R_1 varies from – 0.5 (uniaxial tension) to 1 (equibiaxial) for material within the center pocket region in Fig. 6(f), suggesting the activation of a range of various deformation modes at that location. The pure shear deformation mode was not observed at any point on the panel with the 3D DIC measurement method.

3.2 Deformation Modes and Strain Paths

The DIC experimental results were further analyzed by examining the relationship between true major and minor strains along various section lines at different locations on the T-shape panel. The chosen section lines are shown in Fig. 7(a), as the black segments A-A′, B-B′, C-C′, and D-D′. Segment A-A′, which is 50.6 mm long, runs through the center of the center pocket of the T-shape panel at 25 mm forming depth. The corresponding major and minor strain distributions are shown, respectively, in Figs. 7(b) and (c). The horizontal axis in Fig. 7(b)-(c) is displayed in terms of data points from DIC measurements. For segment A-A′, 140 data points are plotted representing a total length of 50.6mm, with the center position of the center pocket being at 25.3 mm from point A. The maximum true major and minor strains accumulated just outside of the center of the pocket. Hence, positions 1, 2, and 3 which correspond to 27.1 mm (position 1 denoted by the red arrow on segment A-A′), 28.9 mm (position 2 denoted by the purple arrow on segment A-A′), and 31.4 mm (position 3 denoted by the black arrow on segment A-A′), were selected to further investigate the deformation modes and strain paths in the pocket. Figure 7(d) is a plot of major vs. minor strain at positions 1, 2, and 3 on segment A-A′. Specific deformation modes and associated strain paths are denoted by the green dashed line (pure shear), the blue dashed line (pure uniaxial tension), and the purple dashed line (pure equibiaxial tension). Figure 7(d) shows that material at position 1 was subject to equibiaxial tension, material at position 2 was subject to a plane strain deformation mode, while material at position 3 was subject to a uniaxial tension mode. Deformation at positions 1 and 3 followed a linear strain path, while deformation at position 2 followed a non-linear strain path. Figure 7(e) shows that material on section line B-B′ in Fig. 7(a), which is 24.2 mm in length, was subject primarily to plane strain deformation following a

linear strain path associated with pure bending. Figure 7(f) shows the evolution of deformation and strain path along section line C-C′ in Fig. 7(a), which was 23.9 mm in length. Here, material at some points was under uniaxial tension deformation following a linear strain path. However, deformation of material at other points along line C-C′ ranged from uniaxial tension to plane strain to biaxial deformation with non-linear strain paths. It was also noted that some of the C-C′ points followed bilinear strain path wherein plane strain deformation switched to biaxial tension. Figure 7(g) shows that material along line D-D′, which is 39.0 mm in length, was subject to biaxial deformation with both linear and non-linear strain paths as indicated.

3.3 RAVF Measurement Results

Results in Section 3.2 guided the selection of those positions on the T-shaped panel from which specimens were extracted for RAVF measurements using high-energy synchrotron X-ray diffraction. Of the 24 specimens extracted for RAVF measurement, those at the 10 locations shown in Fig. 8(a) from the fully formed T-shaped panel were chosen as representative of all relevant deformation modes and strain paths. Consequently, there was no need to extract specimens from the pocket region for RAVF measurement which was formed late in the stamping process. The ten locations are numbered in Fig. 8(a) (starting from the lower left of the bottom of the T-shape as follows: 9, 8, 2, 3, 12, 14, 20, 21, 23, and 24. Figure 8(b) shows the specific locations of 9, 8, 2, and 3 at the bottom of the T-shape. Figure 8(c) shows the position of specimen 12 at the bottom the T-shape as well as specimen 14 which was extracted from the curved region on the left of the T-shape as shown. Figure 9(d) shows the locations along the head top portion of the T-shape from which specimens 20 and 21 were extracted. Figure

8(e) shows the locations from which specimens 23 and 24 were extracted also from the head of the T-shape.

The RAVF decrease relative to the initial RAVF value of 66 vol.% at each of the 10 locations detailed in Fig. 8 are superimposed on a plot of true major and minor strains (i.e. forming limit diagram space) in Fig. 9 along with the corresponding strain path. Again, specific deformation modes are denoted by the green dashed line (pure shear), the blue dashed line (uniaxial tension), and the purple dashed line (equibiaxial tension). The RAVF decrease was calculated from

$$\Delta RAVF = (RAVF_0 - RAVF_1)/RAVF_0 \quad (3)$$

where $\Delta RAVF$, $RAVF_0$, and $RAVF_1$ are the RAVF decrease, initial RAVF, and RAVF in the fully formed T-shape panel, respectively. The relative size of $\Delta RAVF$ at any one of the 10 locations in Fig. 9 is proportional to the diameter of the corresponding filled circle in the color contour key in Fig. 9. The larger the diameter of a filled circle, the larger the corresponding $\Delta RAVF$ in the fully formed T-shape panel. A curved dotted line runs through each circle. This line has the same color of the circle through which it runs and it denotes a constant effective strain, ε_{eff}, computed with Eq. (2). The ε_{eff} value for each $\Delta RAVF$ is marked along the right edge of the effective strain line in Fig. 9. For example, the ε_{eff} at location 8 with a $\Delta RAVF$ = 59 % is 0.510 with a green color. In fact, the largest $\Delta RAVF$ and ε_{eff} was measured at location 8 where material was subject to biaxial deformation according to Fig. 9. At location 20, however, the strain level is smaller, with ε_{eff} = 0.133, but the corresponding $\Delta RAVF$ of 53% is significant. Hence, martensite phase transformation is especially sensitive to both the biaxial and tensile deformation

modes during forming of the Med. Mn (10 *wt.*%) T-shaped panel. In addition, the strain path corresponding to location 20 is linear, while that corresponding to location 8 is non-linear. Only an 11% $\Delta RAVF$ is noted at location 14 with very small strains, which experienced a plane strain deformation mode under pure bending. Notice that at location 12, the 47% $\Delta RAVF$ is large but the strain path was linear in a nearly balanced biaxial tension deformation mode with relatively small strains. Linear strain paths are associated only with deformation at locations 3 and 12 in the biaxial range of strains. While the range of effective strains for locations 2, 9, 21, and 23 is limited to $0.301 \leq \varepsilon_{eff} \leq 0.357$ under biaxial deformation, the corresponding values of $\Delta RAVF$ are different and range from 32 % at location 1 to 47 % at location 23. A 29 % change in RAVF is noted at location 24 in the biaxial deformation range.

3.4 $\Delta RAVF$ Dependence on Deformation Mode and Strain Path

Specific results extracted from Fig. 9 are investigated to provide a more in-depth examination of austenite to martensite transformation in the Med. Mn (10 *wt.*%) TRIP steel during the entire stamping process to the 25 mm limit of the die set. These focus on the following effects: 1) deformation mode under a linear strain path, 2) ε_{eff} level under linear and bilinear strain paths, 3) ε_{eff} level under different bilinear strain paths, and 4) linear vs. nonlinear strain paths. Each effect is examined in terms of true major vs. minor strain plots that identify ΔRAVF values and associated strain paths at selected locations in Fig. 9.

3.4.1. Deformation Mode under a Linear Strain Path

Figure 10 considers $\Delta RAVF$ values under the three main deformation modes, viz., tension, plane strain, and biaxial tension. These modes were chosen since they each follow a linear strain path as shown in Fig. 10 and their ε_{eff} values fall within the narrowest range of 0.079 – 0.133 for all $\Delta RAVF$ values having linear strain paths. The largest $\Delta RAVF$ of 53 % occurred under uniaxial tension. Alternatively, ΔRAVF is smallest under plane strain deformation since only an 11 % change was noted, while $\Delta RAVF$ = 19 % occurred under a biaxial tension mode which is intermediate to changes occurring under the other two deformation modes. Of the three deformation modes considered in Fig. 10, a greater amount of austenite transformed to martensite under uniaxial tension following a linear strain path under the narrowest range of ε_{eff}.

3.4.2 $\boldsymbol{\varepsilon_{eff}}$ Level under Linear and Bilinear Strain Paths

Values of $\Delta RAVF$, following linear and bilinear strain paths, are considered in Fig. 11. For each strain path, the largest range of ε_{eff} values is considered for the compared $\Delta RAVF$ values. In Fig. 11(a), locations 3 and 12 in Fig. 7 are considered. The $\Delta RAVF$ varied from 19 % (location 2) to 47 % (location 12), when ε_{eff} increased from 0.113 to 0.169, respectively, following linear strain paths under biaxial tension – both are quite close to equibiaxial tension. Figure 11(a) seems to suggest that the higher the value of ε_{eff}, the more austenite transforms to martensite. In Fig. 11(b), $\Delta RAVF$ = 47 % is also achieved at (location 23) with ε_{eff} = 0.350 under biaxial tension with a bilinear strain path. However, $\Delta RAVF$ = 19 % at the companion point in Fig. 11(b) for location 3 with a linear strain path at ε_{eff} = 0.113. Comparison of the data associated with $\Delta RAVF$ = 47 % in Figs. 11(a) and (b), leads to an interesting observation about the effect of strain path on

$\Delta RAVF$. A large ε_{eff} = 0.35 was required to achieve $\Delta RAVF$ = 47 % at location 23 Fig. 11(b) under a bilinear strain path. Yet the much lower value of ε_{eff} = 0.169 was required to achieve the same $\Delta RAVF$ with a linear strain path at location 12 in Fig. 11(a). This suggests that the biaxial tension deformation mode following a linear strain path to $\Delta RAVF$ = 47 % was more effective at martensite phase transformation since a lower ε_{eff} was required to achieve the same $\Delta RAVF$ as was achieved under the bilinear mode at location 23 in Fig. 11(b).

3.4.3 $\boldsymbol{\varepsilon_{eff}}$ Level under Different Bilinear Strain Paths

Bilinear strain paths in Fig. 9 occurred in one of two ways: (i) with a rapid increase in ε_1 (major strain) followed by a slower increase in ε_1, (ii) a slower initial increase in ε_1 followed by a rapid increase in ε_1. Different bilinear strain paths are called out in Figs. 12(a) and (b). The $\Delta RAVF$ values associated with locations 2 and 24 in Fig. 12(a), 32 % and 29 % , respectively, are similar. Both follow (i), and their bilinear strain paths are nearly coincident resulting in ε_{eff} levels of 0.193 (position 24) and 0.338 (position 2). They suggest that most of the austenite transformation occurred below ε_{eff} = 0.193 with only minimal transformation occurring with additional strain under a similar bilinear strain path associated with location 2. A larger disparity between $\Delta RAVF$ values occurred between the two locations considered in the Fig. 12(b), viz. 59 % at location 8 and 47 % at position 23. Both follow (ii). Here, the ε_{eff} increased from 0.350 (position 23) to 0.510 (position 8). Figure 12(b) suggests that the majority of martensite phase transformation occurred below the ε_{eff} = 0.350. Comparison of the data in Figs. 12(a) and (b) suggests that martensite phase transformation reaches the largest $\Delta RAVF$ under a

biaxial tension deformation mode following a bilinear strain path, characterized by a slower initial increase in ε_1 followed by a rapid increase in ε_1. Moreover, positions on the T-shaped stamping (see Fig. 8(a)) such as 2, 8, 23 and 24 were likely to accumulate the highest ε_{eff}.

3.4.4. Linear vs. Nonlinear Strain Paths

A bilinear stain path is associated with location 2 in Fig. 13(a), i.e. a plane strain deformation mode followed by biaxial tension (case (i) considered in Section 5.5.3). Alternatively, material at position 21 experienced a non-linear strain path. Interestingly, the ΔRAVF , the minor strain, and the ε_{eff} values at locations 2 and 21 are very similar, with only the strain path (i.e. linear vs. non-linear) being the notable difference. Alternatively, three bilinear strain paths leading to ΔRAVF values of 32 %, 43 %, and 47 % are shown in Fig. 13(b). These are: plane strain followed by biaxial tension (location 2, ΔRAVF = 32 %), biaxial tension (location 9, ΔRAVF = 43%) characterized by a rapid increase in ε_1 followed by a slower increase in ε_1, and (nearly) equibiaxial tension followed by a biaxial tension (location 23, ΔRAVF = 47 %) mode. The ε_{eff} values at locations 2, 9, and 23 in Fig. 13(b) are nearly the same, i.e. 0.338, 0.357, and 0.350, respectively. In addition, the ΔRAVF values are similar at locations 9 and 23 i.e. 43% and 47%, respectively, while that at location 2 is smallest (32 %). A comparison of Figs. 13(a) and (b) suggests that austenite transformation to martensite under a biaxial tension deformation mode is more sensitive to changes in the true minor strain, ε_2, than the true major strain, ε_1, since there are only very minimal differences in ε_{eff} levels at the end of stamping. Moreover, when ε_2 levels were comparable at two locations, such as 2 and 21 in Fig. 13(a), similar ΔRAVF values resulted, irrespective of the strain path (i.e. linear or

bilinear). At the highest ε_2 values, such as occurred at locations 9 and 23 in Fig. 13 (b), ΔRAVF significantly increased relative to other strain paths and deformation modes considered in Fig. 13.

4. Summary Remarks

In this paper, state-of-the-art experimental methodologies were combined to determine the influence of deformation modes and strain paths on martensitic transformation during stamping of Med. Mn (10 *wt.*%) TRIP steel panels. The panel geometry was designed to emulate a generic b-pillar. This study was motivated by the need for experimental data to assess material constitutive models in finite element simulations of Gen. 3 steel stamping processes and component performance as well as to guide Gen. 3 steel material selection and implementation. An experimental Med. Mn (10 *wt.*%) TRIP steel sheet material, with an initial RAVF value of 66%, was stamped in a laboratory die set at 1mm/s. Stamping did not produce heating to the point where the martensite phase transformation was affected. This is an idealization of most automotive stamping processes in which no heating is intentionally applied either to the blank or the stamping tools. It is a useful first step that will enable CAE modeling to simplify the stamping processing conditions by eliminating the temperature dependence the martensite phase transformation. Strain measurement was accomplished with a three-camera DIC technique using custom post-processing software. Retained austenite volume fraction was measured with synchrotron X-ray diffraction at locations in a selected panel (from a set of 5) wherein material undergoes uniaxial, plane strain, and biaxial tension deformation modes following linear, bi-linear, and non-linear strain paths. The greatest decrease in RAVF occurred under biaxial tension modes each following a bilinear strain

path. Alternatively, the smallest decrease in RAVF occurred under plane strain deformation mode following a linear strain path.

These results suggest some interesting possibilities for achieving desired levels of local RAVF in a stamped Med. Mn (10 *wt.*%) TRIP part with a given initial RAVF. The first possibility is matching of the steel with a stamping process where a specific deformation and strain path predominate. If a higher level of retained austenite is desired in a stamped part, a stamping process wherein plane strain under pure bending may be of interest. The second possibility resides with locally "adjusting" deformation modes and strain paths in the stamped part by adjusting an existing die geometry to achieve desired local levels of retained austenite and martensite. For example, if a higher level of transformation induced martensite is desired for strength, then perhaps a local geometry change in a die that switches the deformation mode from plane strain to biaxial deformation may be desirable given that such a change does not significantly affect part functionality. These possibilities warrant further investigation.

The measurements detailed in this study should be repeated for Med. Mn TRIP steels with different Mn *wt.*% and corresponding heat treatments (e.g. batch annealed vs. continuous anneal). The tensile flow properties of these materials are likely to differ from those detailed in Appendix A for the Med. Mn (10 *wt.*%) TRIP steel, which was the subject of the present study. This suggests that measured RAVF values from the different deformation modes and strain paths in T-shape panels are likely to differ in magnitude from the values in this paper. The effect of heat generation at stamping speeds in excess of that chosen for this study (1 mm/s) should be explored along with measurement of RAVF values at selected forming depths, rather than only in the final stamped part. Both

will require expansion and enhancements of the existing experimental methodology. The effect of edge fracture on martensite phase transformation during T-shape stamping is especially intriguing. This can be explored with the experimental methods used in this study but starting with a blank containing strategically positioned holes. Accurate measurement of RAVF in the vicinity of the holes both before and after they are generated in the blank is required. This will address the influence of the specific machining/punching technique on austenite to martensite phase transformation in the blank material prior to stamping. Once this is done, the combined 3D DIC and high-energy synchrotron X-ray diffraction techniques can be used. The possibility of measuring RAVF in a T-stamping without having to cut out small specimens should be considered. While there is no evidence in the literature of a residual stress effect on measured RAVF in Gen 3 steels, a significant concern is the effect of texture on the initial RAVF measurement since the X-ray beam would not necessarily be positioned at normal incidence at all locations.

5. Conclusions

The main conclusions from this study are as follows:

(1) Stamping of Med. Mn. (10 *wt.*%) TRIP steel into T-shape panels that emulate the rocker-end of a generic b-pillar generated uniaxial tension, plane strain under pure bending, and biaxial tension deformation modes following linear, bi-linear, and non-linear strain paths.

(2) The variety of deformation modes and strain paths during stamping resulted in substantial variation in the $\Delta RAVF$ (11 – 57 %) relative to the initial RAVF of

66 %. The greatest $\Delta RAVF$ (57 %) occurred under biaxial tension following a bi-linear strain path. The smallest $\Delta RAVF$ (11 %) occurred under plane strain following a linear strain path.

(3) A dependence of martensite phase transformation on deformation mode was noted when a linear strain path is followed under similar effective strain levels. This can be gauged by the corresponding $\Delta RAVF$: uniaxial tension (53%) > biaxial tension (19%) > plane strain (11%).

(4) The lower ε_{eff} level associated with biaxial tension deformation modes under linear strain paths renders the linear strain paths more effective at martensite phase transformation than bilinear strain paths, which requires a higher ε_{eff} level.

(5) Martensite phase transformation reaches the largest $\Delta RAVF$ under a biaxial tension deformation mode following a bilinear strain path characterized by a slower initial increase in ε_1 followed by a rapid increase in ε_1.

(6) Martensite phase transformation under a biaxial-tension deformation mode is more sensitive to changes in the tensile minor strain, ε_2, rather than the tensile major strain, ε_1. This is supported by the observation that there are only very minimal differences in ε_{eff} levels at the end of stamping.

(7) For a Med. Mn. (10 *wt.*%) TRIP steel with a known initial RAVF, the results of this study suggest the possibility that martensite transformation can be manipulated to better control formability, strength, and ductility in stamped parts via one of the two means below:

(a) selecting a steel that is better suited to stamping wherein a specific deformation mode and strain path predominate

(b) locally manipulating deformation modes and strain paths by modifying an existing die geometry to achieve a desired level of retained austenite in a stamped part

Acknowledgements

The synchrotron X-ray diffraction work was conducted at the Advanced Photon Source, a U.S. Department of Energy (DOE) Office of Science User Facility operated for the DOE Office of Science by Argonne National Laboratory under Contract No. DE-AC02-06CH11357. The support of Mr. R. Spence of Argonne Beam Line 11-I-DC during all phases of the synchrotron study is gratefully acknowledged. R. Alturk and C.M. Enloe assisted with measurement of the Med. Mn (10 *wt.*%) TRIP tensile flow properties. W.W., YW.W., P. M., F. Z., and G.A.T. acknowledge the support of the AK Steel Corporation. This material is based upon work supported by the Department of Energy National Energy Technology Laboratory under Award Number No. DE-EE0005976. This report was prepared as an account of work sponsored by an agency of the United States Government. Neither the United States Government nor any agency thereof, nor any of their employees, makes any warranty, express or implied, or assumes any legal liability or responsibility for the accuracy, completeness, or usefulness of any information, apparatus, product, or process disclosed, or represents that its use would not infringe privately owned rights. Reference herein to any specific commercial product, process, or service by trade name, trademark, manufacturer, or otherwise does not necessarily constitute or imply its endorsement, recommendation, or favoring by the United States Government or any agency thereof. The views and opinions of authors expressed herein do not necessarily state or reflect those of the United States Government or any agency thereof. Such support does not constitute an endorsement by the Department of Energy of the work or the views expressed herein.

References

[1] E. DeMoor, P.J. Gibbs, J.G. Speer, D.K. Matlock, Strategies for Third Generation Advanced High Strength Steel Development, AIST Trans. 7(3) (2010) 133-144.

[2] B.C. De Cooman, K.-g. Chin, S.-J. Kim, High Mn TWIP Steels for Automotive Applications, 3rd ed.2011.

[3] V.F. Zackay, E.R. Parker, D. Fahr, R. Bush, The enhancement of ductility in high strength steels, Tran. Am. Soc. of Met. 60 (1967) 252-259.

[4] G.B. Olson, M. Cohen, Kinetics of Strain-Induced Martensitic Nucleation, Metall. Mater. Trans. A 6 (1975) 791-795.

[5] B.C. De Cooman, P. Gibbs, S. Lee, D.K. Matlock, Transmission Electron Microscopy Analysis of Yielding in Ultrafine-Grained Medium Mn

Transformation-Induced Plasticity Steel, Metall. Mater. Trans. A 44(6) (2013) 2563-2572.

[6] S. Martin, C. Ullrich, D. Rafaja, Deformation of Austenitic CrMnNi TRIP/TWIP Steels: Nature and Role of the ε−martensite, Mater. Today 2 (2015) S643-S646.

[7] Z.Y. Liang, Y.Z. Li, M.X. Huang, The respective hardening contributions of dislocations and twins to the flow stress of a twinning-induced plasticity steel, Scr. Mater. 112 (2016) 28-31.

[8] B.C. De Cooman, O. Kwon, K.G. Chin, State-of-the-knowledge on TWIP steel, Mater. Sci. Tech. 28(5) (2012) 513-527.

[9] D. Pérez Escobar, S. Silva Ferreira de Dafé, D. Brandão Santos, Martensite reversion and texture formation in 17Mn-0.06C TRIP/TWIP steel after hot cold rolling and annealing, J. Mater. Res. Tech. 4(2) (2015) 162-170.

[10] B.C. De Cooman, High Mn TWIP steel and medium Mn steel, Woodhead 2016.

[11] S. Martin, S. Wolf, U. Martin, L. Krüger, D. Rafaja, Deformation Mechanisms in Austenitic TRIP/TWIP Steel as a Function of Temperature, Metall. Mater. Trans. A 47(1) (2016) 49-58.

[12] P.J. Gibbs, E. De Moor, M.J. Merwin, B. Clausen, J.G. Speer, D.K. Matlock, Austenite Stability Effects on Tensile Behavior of Manganese-Enriched-Austenite Transformation-Induced Plasticity Steel, Metall. Mater. Trans. A 42(12) (2011) 3691-3702.

[13] A. Bachmaier, K. Hausmann, D. Krizan, A. Pichler, Development of TBF steels with 980 MPa tensile strength for automotive applications: microstructure and mechanical properties, Proceedings of the International Symposium on New Developments in Advanced High-strength Steels (2013) 13-139.

[14] A.J. Clarke, J.G. Speer, M.K. Miller, R.E. Hackenberg, D.V. Edmonds, D.K. Matlock, F.C. Rizzo, K.D. Clarke, E. De Moor, Carbon partitioning to austenite from martensite or bainite during the quench and partition (Q&P) process: A critical assessment, Acta Mater. 56(1) (2008) 16-22.

[15] B. Sun, F. Fazeli, C. Scott, S. Yue, Phase Transformation Behavior of Medium Manganese Steels with 3 Wt Pct Aluminum and 3 Wt Pct Silicon During Intercritical Annealing, Metall. Mater. Trans. A 47(10) (2016) 4869-4882.

[16] Y.K. Lee, J. Han, Current opinion in medium manganese steel, Mater. Sci. Tech. 31(7) (2015) 843-856.

[17] A. Ito, A. Shibata, N. Tsuji, Thermomechanical Processing of Medium Manganese Steels, Mater. Sci. Forum 879 (2017) 90-94.

[18] C.D. Horvath, C.M. Enloe, J.P. Singh, J.J. Coryell, Persistent Challenges to Advanced High Strength Steel Implementation, 3rd ed., Keystone, CO, Association for Iron & Steel Technology, 2017.

[19] X.C. Xiong, B. Chen, M.X. Huang, J.F. Wang, L. Wang, The effect of morphology on the stability of retained austenite in a quenched and partitioned steel, Scr. Mater. 68(5) (2013) 321-324.

[20] W. Poling, V. Savic, J. Hector, L. G. , A.K. Sachdev, X. Hu, A. Devaraj, X. Sun, F. Abu-Farha, Combined Synchrotron X-ray Diffraction and Digital Image Correlation Technique for Measurement of Austenite Transformation with Strain in TRIP-assisted Steels, SAE Tech. Paper (2016) 2016-01-0419.

[21] D.M. Collins, T. Erinosho, F.P.E. Dunne, R.I. Todd, T. Connolley, M. Mostafavi, H. Kupfer, A.J. Wilkinson, A synchrotron X-ray diffraction study of non-proportional strain-path effects, Acta Mater. 124 (2017) 290-304.
[22] T. Gnäupel-Herold, A. Creuziger, Diffraction study of the retained austenite content in TRIP steels, Mat. Sci. Eng. A 528(10–11) (2011) 3594-3600.
[23] P.J. Jacques, S. Allain, O. Bouaziz, A. De, A.-F. Gourgues, B.M. Hance, Y. Houbaert, J. Huang, A. Iza-Mendia, S.E. Kruger, M. Radu, L. Samek, J. Speer, L. Zhao, S. van der Zwaag, On measurement of retained austenite in multiphase TRIP steels — results of blind round robin test involving six different techniques, Mater. Sci. Tech. 25 (2009) 567-574.
[24] S.F. Peterson, M.C. Mataya, D.K. Matlock, The formability of austenitic stainless steels, JOM 49(9) (1997) 54.
[25] J. Coryell, V. Savic, J. Hector, L. G., S. Mishra, Temperature Effects on the Deformation and Fracture of a Quenched-and-Partitioned Steel, SAE Tech. Paper (2013) 2013-01-0610.
[26] N.H. van Dijk, A.M. Butt, L. Zhao, J. Sietsma, S.E. Offerman, J.P. Wright, S. van der Zwaag, Thermal stability of retained austenite in TRIP steels studied by synchrotron X-ray diffraction during cooling, Acta Mater. 53(20) (2005) 5439-5447.
[27] J. Van Slycken, P. Verleysen, J. Degrieck, L. Samek, B.C. de Cooman, High-strain-rate behavior of low-alloy multiphase aluminum- and silicon-based transformation-induced plasticity steels, Metall. Mater. Trans. A 37(5) (2006) 1527-1539.
[28] T. Iwamoto, T. Tsuta, Y. Tomita, Investigation on deformation mode dependence of strain-induced martensitic transformation in trip steels and modelling of transformation kinetics, Inter. J. Mech. Sci. 40(2) (1998) 173-182.
[29] H. Li, Y. Zhang, W. Zhao, Z. Gu, X. Li, J. Ma, TRIP steel retained austenite transformation under cyclic V-bending deformation, J. Wuhan. Uni. Tech.-Mater. Sci. Ed. 29(3) (2014) 594-600.
[30] S.T. Oh, K.K. Park, H.-N. Han, S.-H. Park, K.H. Oh, Transformation behavior of retained austenite in hydroformed TRIP steel, Mater. Sci. Forum 408-412 (2002) 1341-1346.
[31] T.K. Shan, S.H. Li, W.G. Zhang, Z.G. Xu, Prediction of martensitic transformation and deformation behavior in the TRIP steel sheet forming, Mater. Des. 29(9) (2008) 1810-1816.
[32] K.-i. Sugimoto, K. Nakano, S.-M. Song, T. Kashima, Retained Austenite Characteristics and Stretch-flangeability of High-strength Low-alloy TRIP Type Bainitic Sheet Steels, ISIJ Inter. 42(4) (2002) 450-455.
[33] M.R. Berrahmoune, S. Berveiller, K. Inal, A. Moulin, E. Patoor, Analysis of the martensitic transformation at various scales in TRIP steel, Mat. Sci. Eng. A 378(1–2) (2004) 304-307.
[34] R. Blondé, E. Jimenez-Melero, L. Zhao, J.P. Wright, E. Brück, S. van der Zwaag, N.H. van Dijk, Mechanical stability of individual austenite grains in TRIP steel studied by synchrotron X-ray diffraction during tensile loading, Mat. Sci. Eng. A 618 (2014) 280-287.

[35] S. Cheng, X.-L. Wang, Z. Feng, B. Clausen, H. Choo, P.K. Liaw, Probing the Characteristic Deformation Behaviors of Transformation-Induced Plasticity Steels, Metall. Mater. Trans. A 39(13) (2008) 3105.
[36] J. Hu, W. Cao, C. Wang, H. Dong, J. Li, Austenite Stability and Its Effect on the Ductility of the Cold-rolled Medium-Mn Steel, ISIJ Inter. 54(8) (2014) 1952-1957.
[37] A. Kromm, S. Brauser, T. Kannengiesser, M. Rethmeier, High-energy synchrotron diffraction study of a transformation induced plasticity steel during tensile deformation, J. Strain Anal. Eng. Des. 48 (2011) 589-591.
[38] O. Muránsky, P. Lukáš, J. Zrník, P. Šittner, Neutron diffraction analysis of retained austenite stability in Mn–Si steel during plastic deformation, Physica B 385–386, Part 1 (2006) 587-589.
[39] K.-i. Sugimoto, N. Usui, M. Kobayashi, S.-i. Hashimoto, Effects of Volume Fraction and Stability of Retained Austenite on Ductility of TRIP-aided Dual-phase Steels, ISIJ Inter. 32(12) (1992) 1311-1318.
[40] J. Zrník, O. Muránsky, P. Lukáš, Z. Nový, P. Sittner, P. Horňak, Retained austenite stability investigation in TRIP steel using neutron diffraction, Mat. Sci. Eng. A 437(1) (2006) 114-119.
[41] W. Wu, K. An, Understanding low-cycle fatigue life improvement mechanisms in a pre-twinned magnesium alloy, J. Alloys Comp. 656 (2016) 539-550.
[42] W. Wu, K. An, L. Huang, S.Y. Lee, P.K. Liaw, Deformation dynamics study of a wrought magnesium alloy by real-time in situ neutron diffraction, Scr. Mater. 69(5) (2013) 358-361.
[43] W. Wu, C.-P. Chuang, D. Qiao, Y. Ren, K. An, Investigation of deformation twinning under complex stress states in a rolled magnesium alloy, J. Alloys Comp. 683 (2016) 619-633.
[44] W. Wu, Y. Gao, N. Li, C.M. Parish, W. Liu, P.K. Liaw, K. An, Intragranular twinning, detwinning, and twinning-like lattice reorientation in magnesium alloys, Acta Mater. 121 (2016) 15-23.
[45] W. Wu, S.Y. Lee, A.M. Paradowska, Y.F. Gao, P.K. Liaw, Twinning-detwinning behavior during fatigue-crack propagation in a wrought magnesium alloy AZ31B, Mater. Sci. Eng. A-Struct. Mater. Prop. Microstruct. Process. 556 (2012) 278-286.
[46] W. Wu, P.K. Liaw, K. An, Unraveling cyclic deformation mechanisms of a rolled magnesium alloy using in situ neutron diffraction, Acta Mater. 85 (2015) 343-353.
[47] W. Wu, H. Qiao, K. An, X.Q. Guo, P.D. Wu, P.K. Liaw, Investigation of deformation dynamics in a wrought magnesium alloy, Int. J. Plast. 62 (2014) 105-120.
[48] H.Y. Yu, G.Y. Kai, M. De Jian, Transformation behavior of retained austenite under different deformation modes for low alloyed TRIP-assisted steels, Mat. Sci. Eng. A 441(1–2) (2006) 331-335.
[49] C.F. Jatczak, Retained austenite and its measruement by X-Ray diffraction, SAE Tech. Paper (1980) 800426.
[50] K.S. Choi, W.N. Liu, X. Sun, M.A. Khaleel, Microstructure-based constitutive modeling of TRIP steel: Prediction of ductility and failure modes under different loading conditions, Acta Mater. 57(8) (2009) 2592-2604.

[51] P.J. Jacques, Q. Furnémont, F. Lani, T. Pardoen, F. Delannay, Multiscale mechanics of TRIP-assisted multiphase steels: I. Characterization and mechanical testing, Acta Mater. 55(11) (2007) 3681-3693.
[52] J. Kobayashi, D.V. Pham, K. Sugimoto, Stretch-flangeability of 1.5GPa grade TRIP-aided martensitic cold rolled sheet steels, Steel Res. Inter. (2011) 598-603.
[53] K.-i. Sugimoto, A.K. Srivastava, Microstructure and Mechanical Properties of a TRIP-Aided Martensitic Steel, Metal. Micro. Anal. 4(5) (2015) 344-354.
[54] G. Lacroix, T. Pardoen, P.J. Jacques, The fracture toughness of TRIP-assisted multiphase steels, Acta Mater. 56(15) (2008) 3900-3913.
[55] C.G. Lee, S.-J. Kim, T.-H. Lee, S. Lee, Effects of volume fraction and stability of retained austenite on formability in a 0.1C–1.5Si–1.5Mn–0.5Cu TRIP-aided cold-rolled steel sheet, Mat. Sci. Eng. A 371(1–2) (2004) 16-23.
[56] M.P. Pereira, B.F. Rolfe, Temperature conditions during 'cold' sheet metal stamping, J. Mater. Process. Tech. 214(8) (2014) 1749-1758.
[57] F. Chen, X. Chen, X. Xie, X. Feng, L. Yang, Full-field 3D measurement using multi-camera digital image correlation system, Opt. Laser. Eng. 51(9) (2013) 1044-1052.
[58] J. Li, X. Xie, G. Yang, B. Zhang, T. Siebert, L. Yang, Whole-field thickness strain measurement using multiple camera digital image correlation system, Opt. Laser. Eng. 90 (2017) 19-25.
[59] C. Chovan, B. Mengiste, X. Chen, L. Yang, Improving material property measurement by using multi-camera digital image correlation, SAE Tech. Paper (2013) 2013-01-1428.
[60] DANTEC DYNAMICS ISTRA 4D, http://www.dantecdynamics.com/istra-4d-shearography. http://www.dantecdynamics.com/istra-4d-shearography.
[61] Igor Pro Softeware, https://www.wavemetrics.com/index.html.
[62] B.R. Deis, Thickness strain analysis as a tool for process control in metal forming, SAE Tech. Paper (1990) 900279.
[63] A. Moreau, D. Lévesque, M. Lord, M. Dubois, J.P. Monchalin, C. Padioleau, J.F. Bussière, On-line measurement of texture, thickness and plastic strain ratio using laser-ultrasound resonance spectroscopy, Ultrasonics 40(10) (2002) 1047-1056.
[64] Y.W. Wang, Investigation of AHSS Formability Using a Customized T-Shaped Panel with ex-situ DIC, GDIS (2016).
[65] T. Altan, A.E. Takaya (eds), Sheet metal forming fundametals, ASM Inter. 2012.
[66] N.A. Zanjani, A. Dervaric, S. Kalyanasundaram, A novel buckling indicator using the correlation between in-plane and out-of-plane displacement, Int. J. Eng. Res. Tech. 3(10) (2014) 1054-1061.
[67] X.H. Hu, X. Sun, L.G. Hector Jr, Y. Ren, Individual phase constitutive properties of a TRIP-assisted QP980 steel from a combined synchrotron X-ray diffraction and crystal plasticity approach, Acta Mater. 132 (2017) 230-244.
[68] Y. Wang, H. Xu, D.L. Erdman, M.J. Starbuck, S. Simunovic, Characterization of High-Strain Rate Mechanical Behavior of AZ31 Magnesium Alloy Using 3D Digital Image Correlation, Adv. Eng. Mater. 13(10) (2011) 943-948.
[69] X. Yang, L.G. Hector, J. Wang, A Combined Theoretical/Experimental Approach for Reducing Ringing Artifacts in Low Dynamic Testing with Servo-hydraulic Load Frames, Exp. Mech. 54(5) (2014) 775-789.

[70] V. Savic, M. Pawlicki, P.E. Krajewski, M. Voss, J. Hector, L.G. , K.S. Snavely, Passive Pedestrian Protection Approach for Vehicle Hoods, SAE Tech. Paper (2014) 2014-01-0513.
[71] P.D. Zavattieri, V. Savic, L.G. Hector, J.R. Fekete, W. Tong, Y. Xuan, Spatio-temporal characteristics of the Portevin–Le Châtelier effect in austenitic steel with twinning induced plasticity, Int. J. Plast. 25(12) (2009) 2298-2330.
[72] S. Lee, B.C. De Cooman, Tensile Behavior of Intercritically Annealed Ultra-Fine Grained 8% Mn Multi-Phase Steel, Steel Res. Inter. 86(10) (2015) 1170-1178.
[73] Z.Y. Tang, R.D.K. Misra, M. Ma, N. Zan, Z.Q. Wu, H. Ding, Deformation twinning and martensitic transformation and dynamic mechanical properties in Fe–0.07C–23Mn–3.1Si–2.8Al TRIP/TWIP steel, Mat. Sci. Eng. A 624 (2015) 186-192.
[74] M. Isakov, S. Hiermaier, V.-T. Kuokkala, Effect of Strain Rate on the Martensitic Transformation During Plastic Deformation of an Austenitic Stainless Steel, Metall. Mater. Trans. A 46(6) (2015) 2352-2355.
[75] P.M. Edwards, Origin 7.0: Scientific Graphing and Data Analysis Software, J. Chem. Info. Comp. Sci. 42(5) (2002) 1270-1271.
[76] C. Kim, X-ray method of measuring retained austenite in heat treated white cast irons, J. Heat Treat. 1(2) (1979) 43-51.

TABLE

Table 1 Chemical composition in weight percentage (*wt.*%) of Med. Mn (10 *wt.*%) steel.

Elements	Mn	C	Al	Si	Sn	P	S	Co	Cr	Fe
wt.%	9.76	0.16	1.37	0.19	0.003	0.002	0.0018	< 0.002	< 0.002	Balance

FIGURES

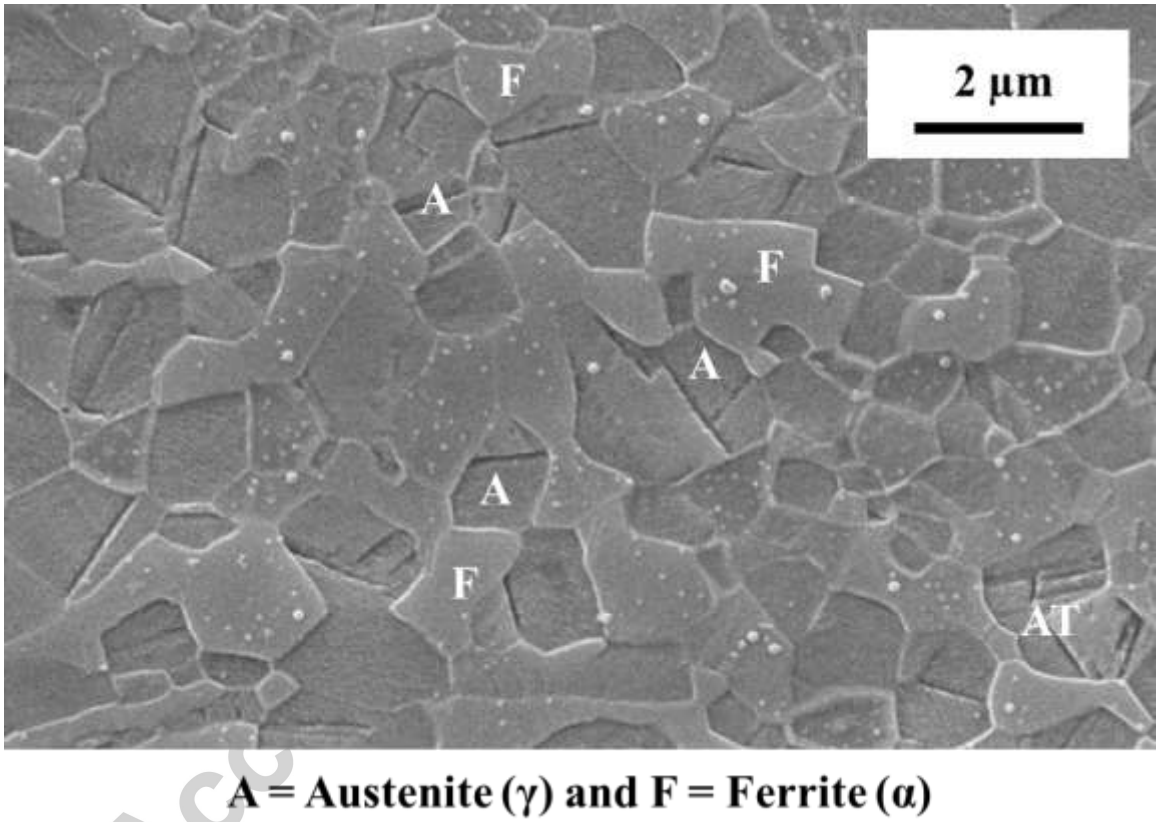

Figure 1 Field emission SEM image of the as-received 10 *wt.*% medium Mn TRIP steel [two phase, ferrite (F) and retained austenite (A)] with approximately 2 µm grain size. Some annealing twins (AT) were observed in the austenite grains which are indicative of a low stacking fault energy.

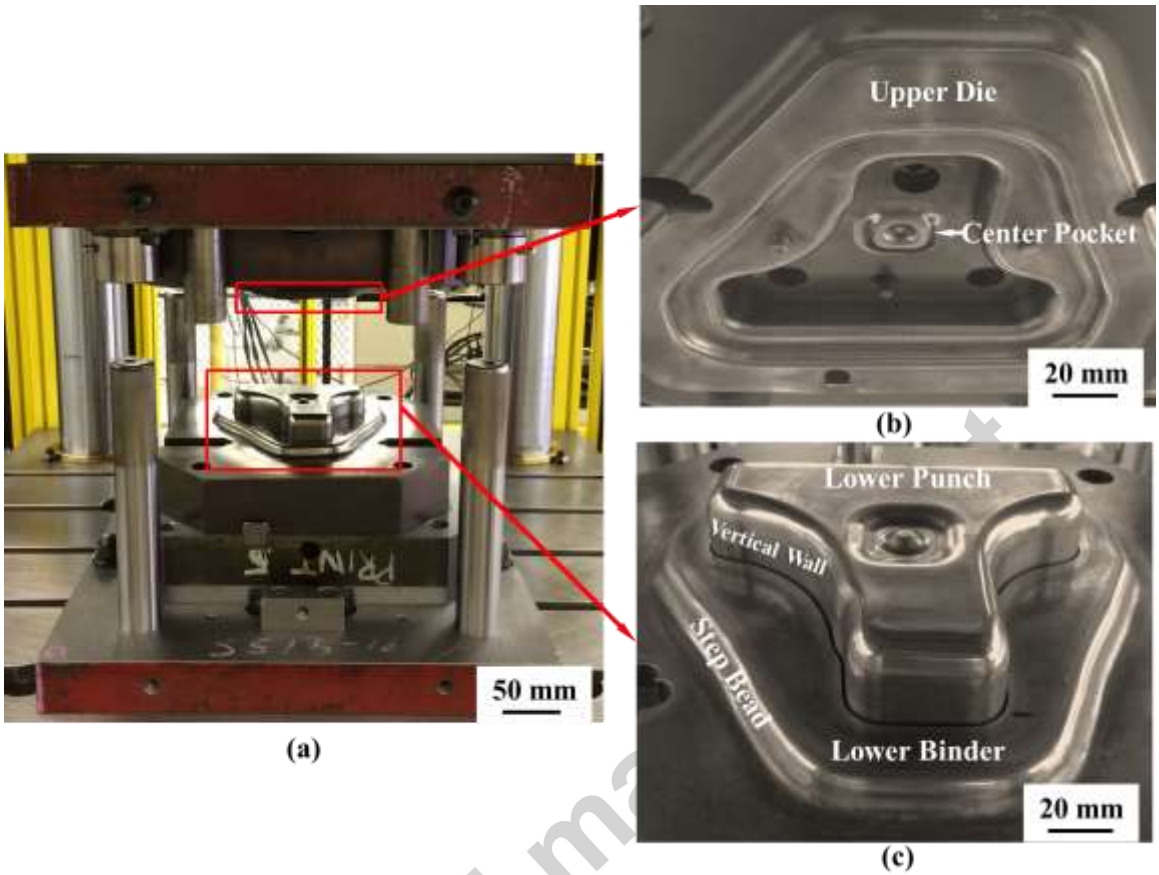

Figure 2 (a) The T-shaped stamping die set in the double-action Interlaken press. (b) Close-up view of the upper die showing the center pocket region. (c) Close-up view of the lower punch showing the center pocket region.

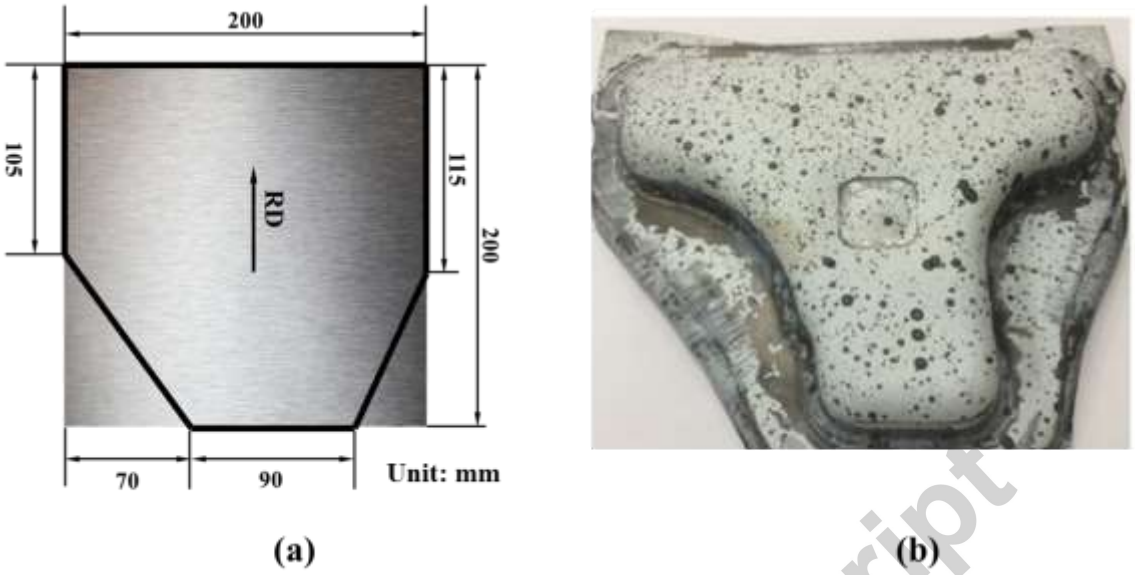

Figure 3 (a) Blank geometries (denoted by a solid black boundary). All dimensions in mm. The rolling direction is denoted by RD. The top of the T-shape is formed from the 200 mm end, while the bottom of the T-shape is formed from the 90 mm end. (b) The outer surface of T-shape stamping formed to maximum 25 mm depth with DIC contrast pattern consisting of black spray paint droplets on top of the white spray paint applied to the flat blank.

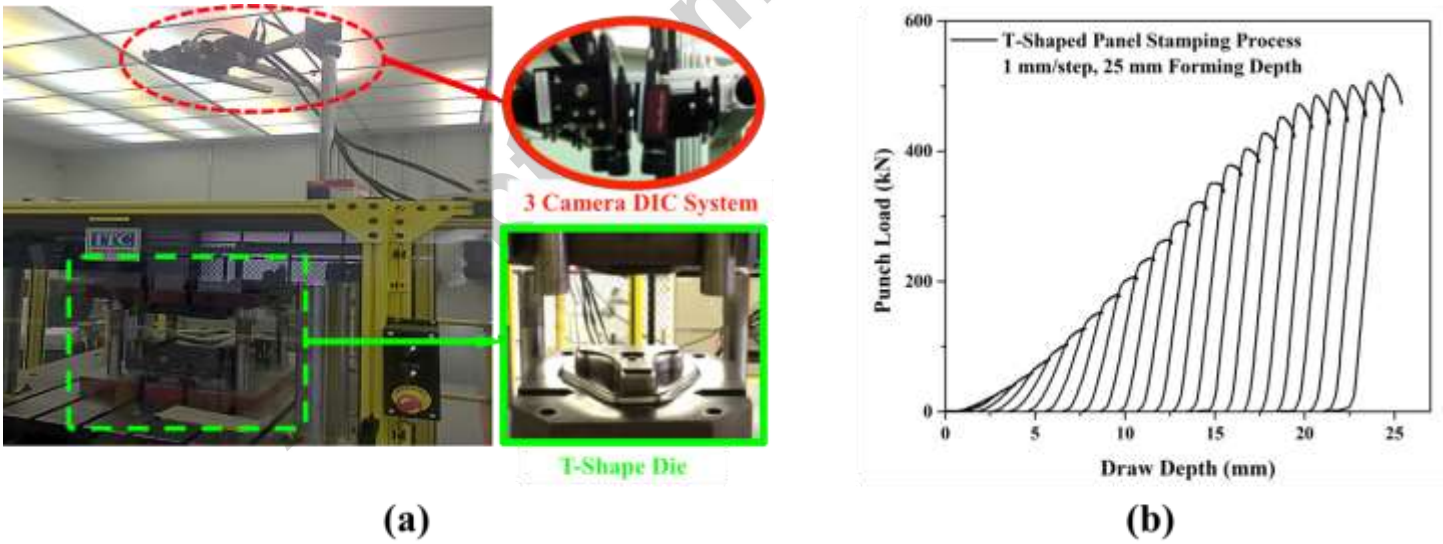

Figure 4 (a) Image of the three-camera digital image correlation system affixed above the Interlaken press. (b) Load-displacement curves from interrupted forming (1 mm depth per step) of T-shaped stampings formed without and with punched holes.

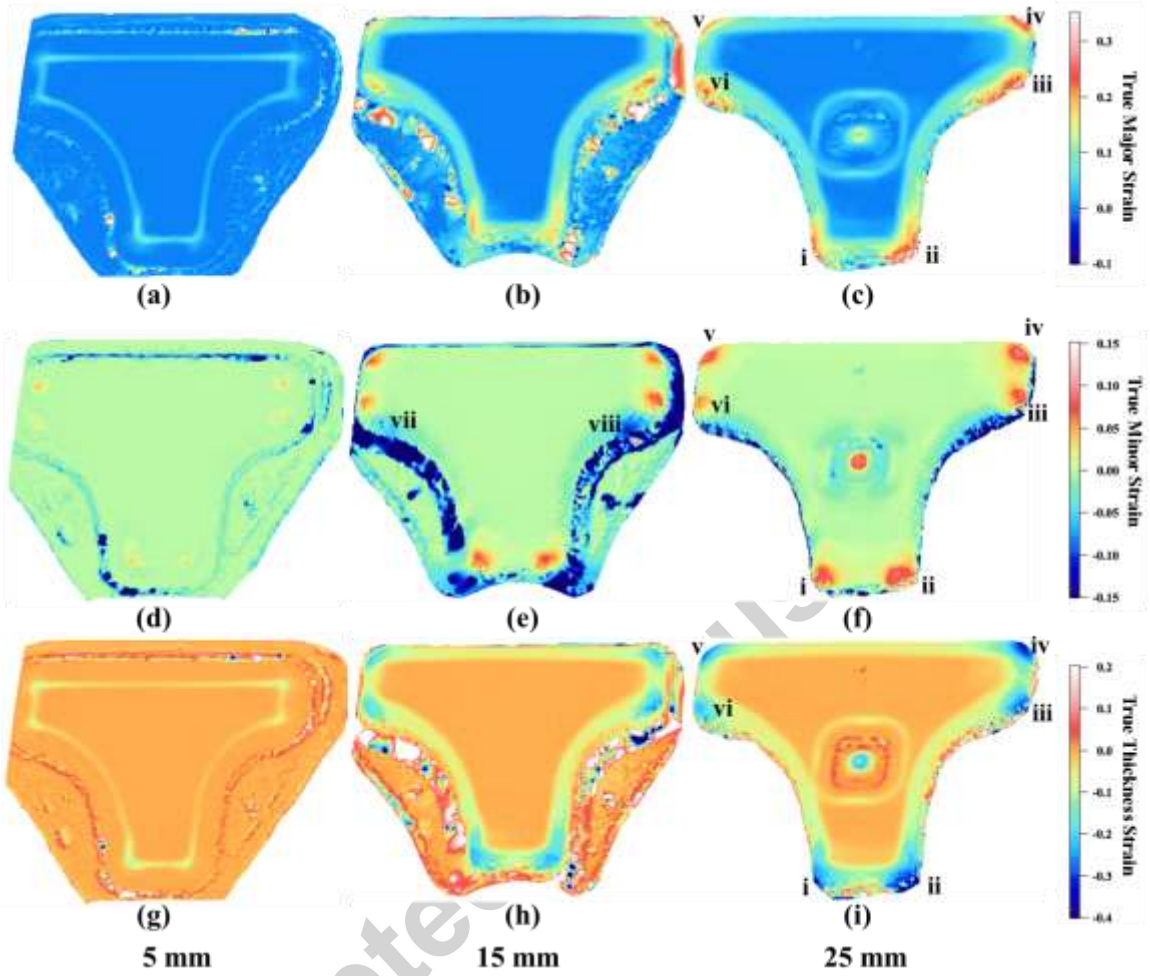

Figure 5 Major (a)-(c), minor (d)-(f), and calculated thickness [Eq. (1), (g)-(i)] true strain fields, at 5, 15, and 20 mm forming depths, respectively, on the outer surface of a Med. Mn (10 *wt.*%) TRIP T-shape panel. As expected, peak strain accumulation occurs at the corners of the T-shape denoted by i-vi in (c), (f), and (i). The compressive minor strain were observed at vii and viii marked on (e). Note that the white regions are indicative of artifacts from the DIC measurement due to loss of the contrast pattern during stamping. These artifacts in no way affected the strains used to investigate RAVF dependence on deformation and strain path.

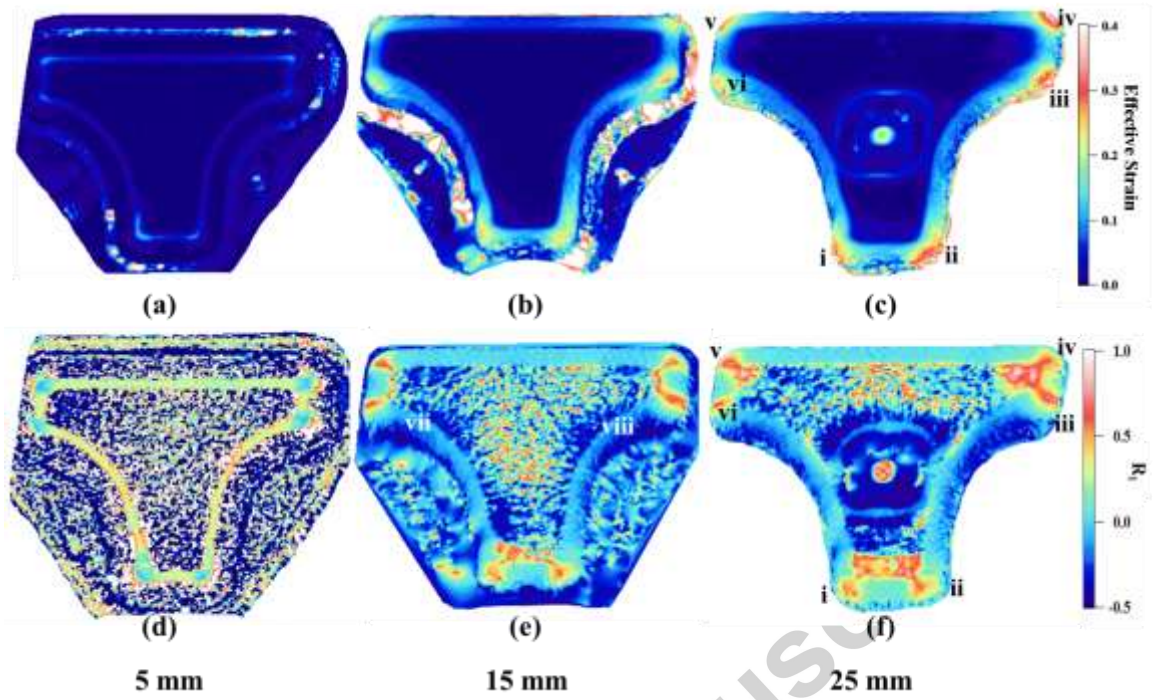

Figure 6 (a)-(c) The calculated ε_{eff} field [Eq. (2)] at 5, 15, and 25 mm forming depth on the T-shape panel, respectively. This information calls out the locations of peak strain accumulation during stamping. (d)-(f) The deformation mode distribution in terms of calculated $R_1 = \varepsilon_2 / \varepsilon_1$ contours at 5, 15, and 25 mm forming depth. The value of $R_1 = -0.5$, 0, and 1 represent uniaxial tension, plane strain, and equibiaxial tension deformation mode, respectively.

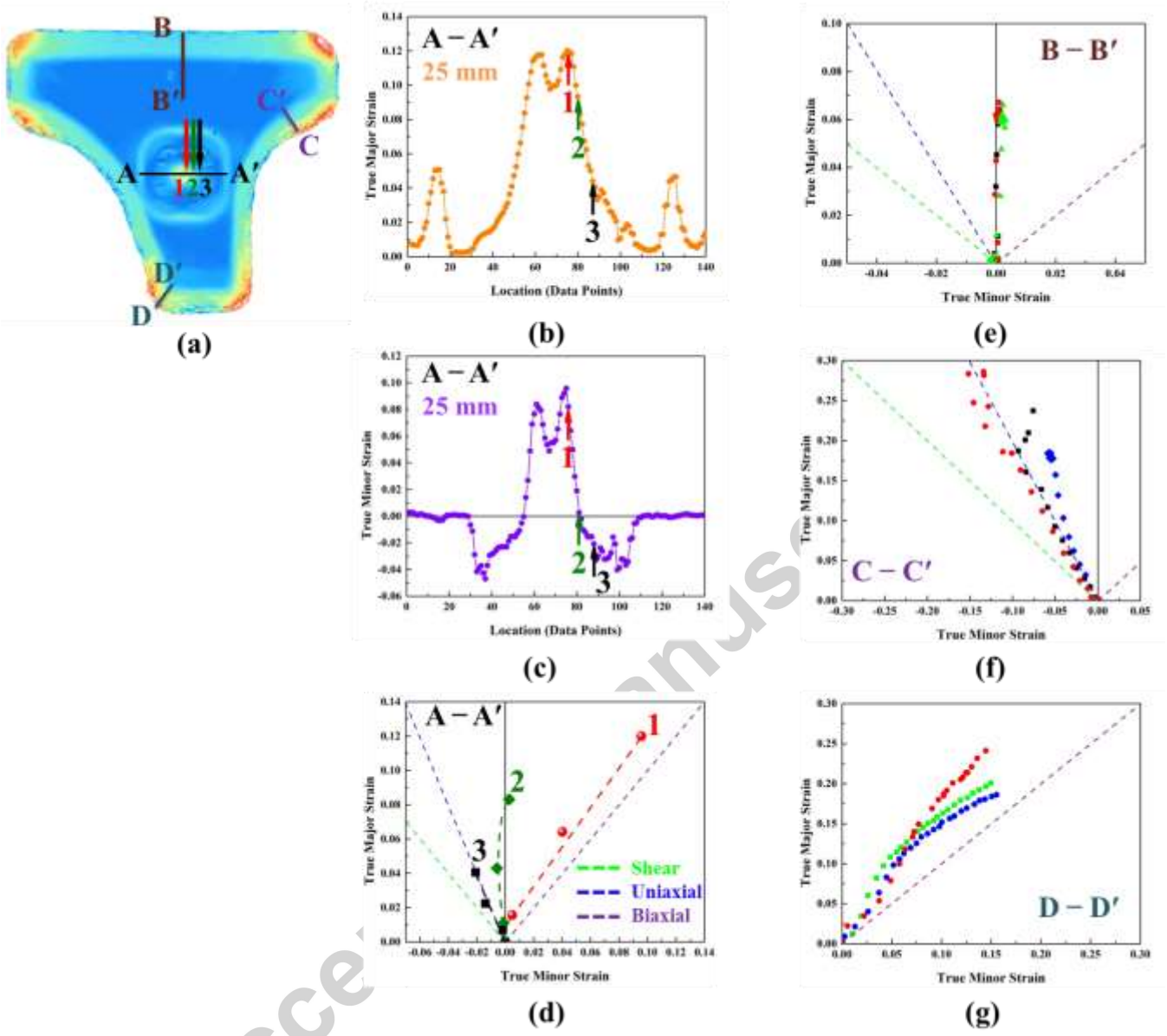

Figure 7 (a) The major strain distribution in Fig. 5(c) at 25 mm forming depth with segments A-A′ (50.6 mm), B-B ′ (24.2 mm), C-C ′(23.9 mm), and D-D ′ (39.0 mm) called out on the T-shape panel. The arrows denote points along segment A-A′ within the pocket region of the stamping considered in Fig. 7 (b)-(d). The true major (b) and minor (c) strain distributions from DIC along segment A-A′ in (a) in terms of data points (50.6 mm = 140 data points) at the 25 mm forming depth. The dashed lines denote shear (green), uniaxial tension (blue), and equibiaxial tension (purple). (d) The evolution of deformation modes and strain paths for locations 1, 2, and 3 marked on segment A-A′ in (a). (e)-(g) Strain path and deformation mode evolution for B-B′, C-C′, and D-D′ segments at selected locations, respectively, during forming. The deformation mode along B-B′ is primarily plane strain. Deformation modes along C-C′ change from non-equibiaxial at small strains, to plane strain to tension at the largest strains. Deformation modes along segment D-D′ are initially equibiaxial tension at the smallest strains and then non-equibiaxial at the largest strains.

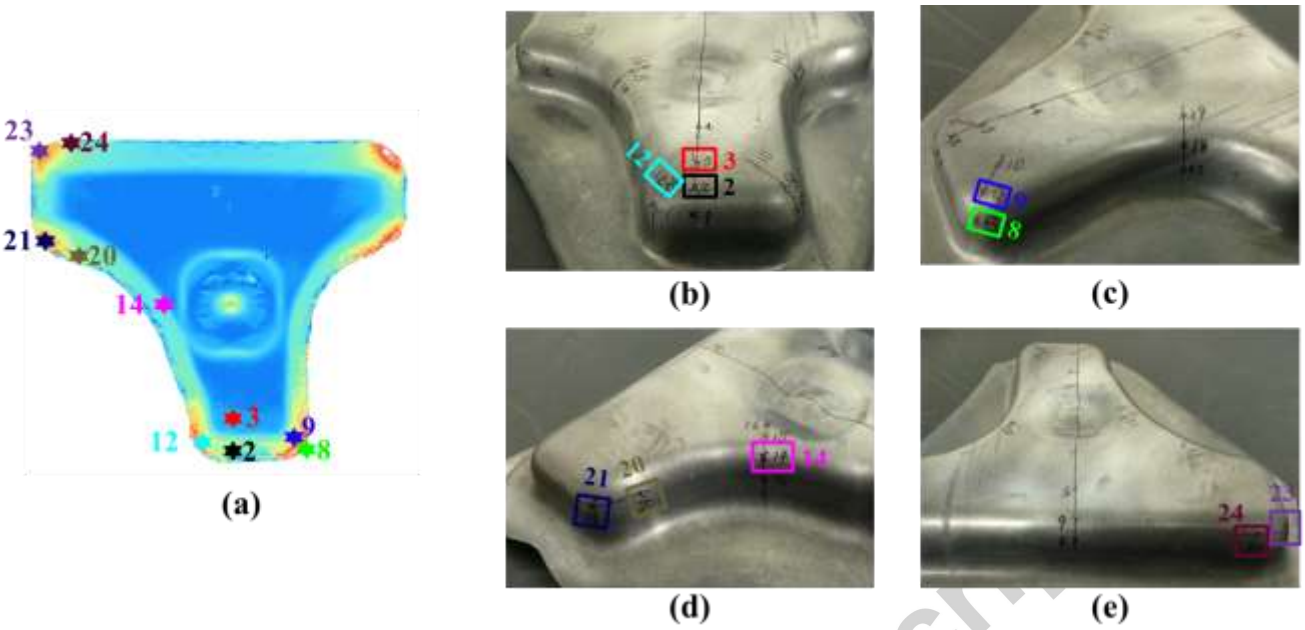

Figure 8 (a) Figure 5(c) (major true strain contours from DIC) with the 10 of the 24 locations at which RAVF was measured with synchrotron X-ray diffraction denoted. Moving clockwise around the bottom of the T: (b) Locations 2, 3, and 12, (c) Locations 8 and 9, (d) Locations 14, 20 and 21, (e) Locations 23 and 24.

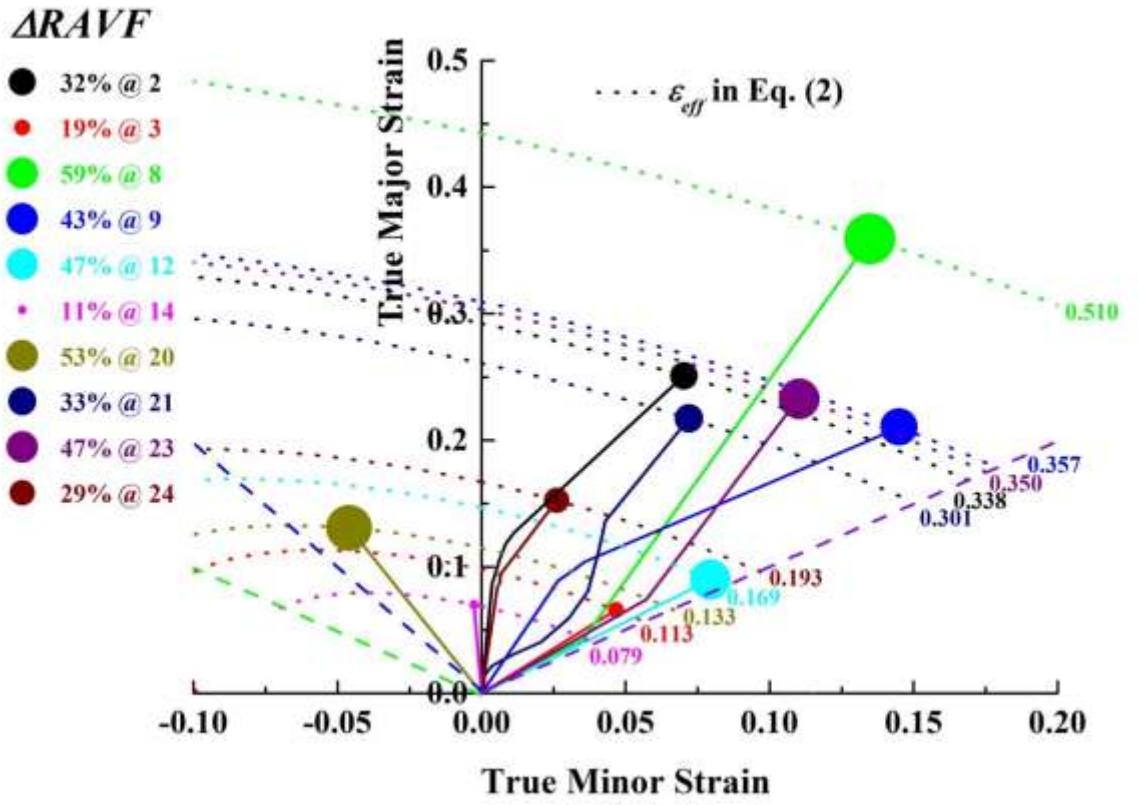

Figure 9 Variation $\Delta RAVF$ [relative to the initial 66 % RAVF, see Eq. (3)] with major and minor true strains at the 10 locations identified in Fig. 8(a). The larger the diameter of a colored circle is, the greater the measured RAVF decrease. The dashed (straight) lines denote shear (green), uniaxial tension (blue), and equibiaxial tension (purple) deformation modes. Dotted (curved) lines denote calculated ε_{eff} [see Eq. (2)] levels using DIC-measured true strains. Each is associated with a specific $RAVF$.

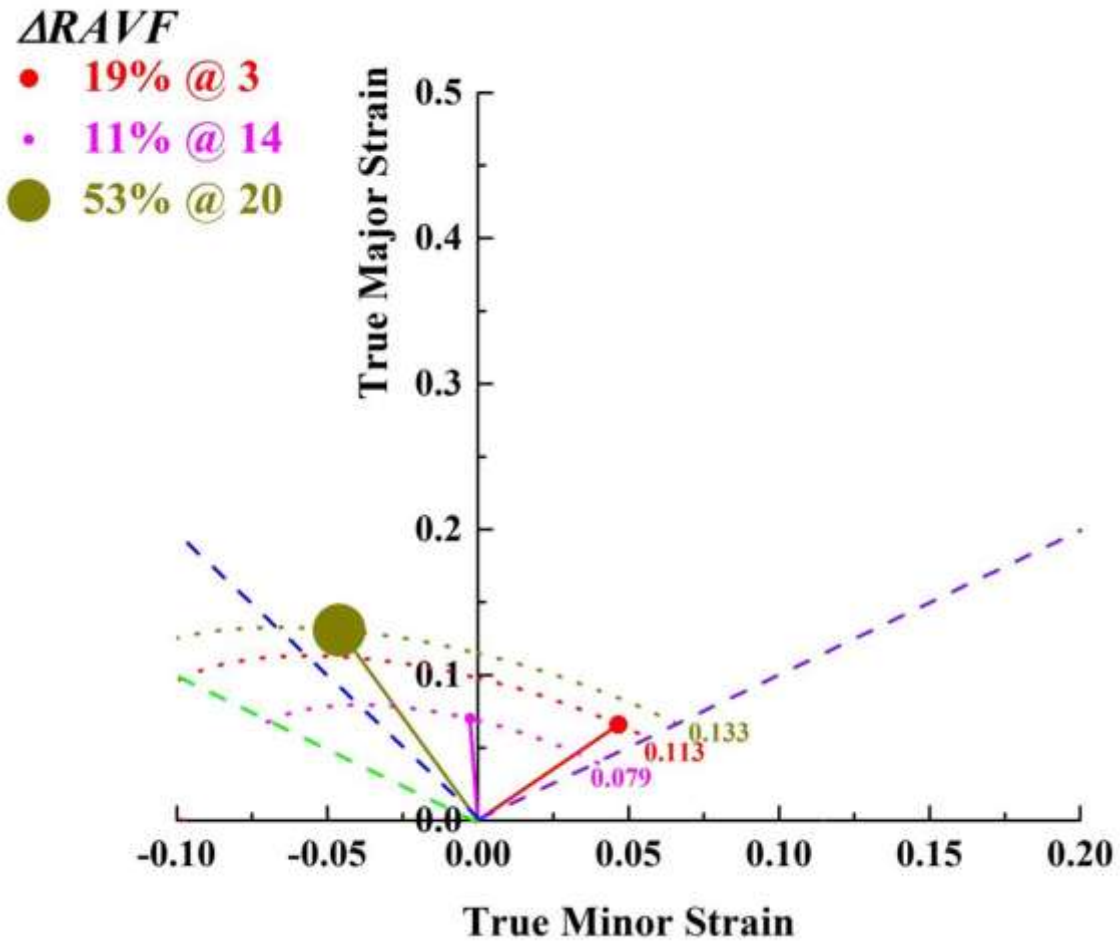

Figure 10 Effect of deformation modes on $\Delta RAVF$ [see Eq. (3)] under the linear strain path. The dashed (straight) lines denote shear (green), uniaxial tension (blue), and equibiaxial tension (purple) deformation modes. Dotted (curved) lines denote calculated ε_{eff} [see Eq. (2)] levels using DIC-measured true strains. Each is associated with a specific $RAVF$.

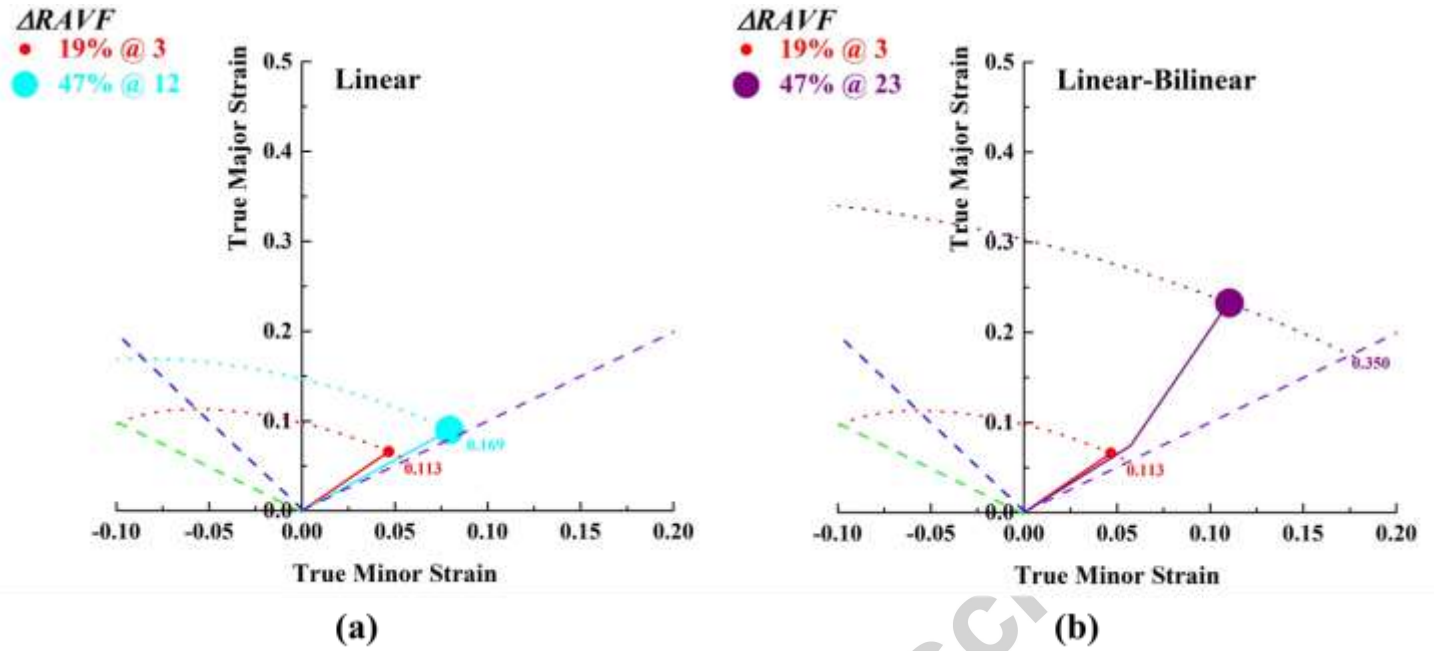

Figure 11 The ε_{eff} level effect on $\Delta RAVF$ [see Eq. (3)] under linear (a) and bilinear (b) strain paths. The dashed (straight) lines denote shear (green), uniaxial tension (blue), and equibiaxial tension (purple) deformation modes. Dotted (curved) lines denote calculated ε_{eff} [see Eq. (2)] levels using DIC-measured true strains. Each is associated with a specific $\Delta RAVF$.

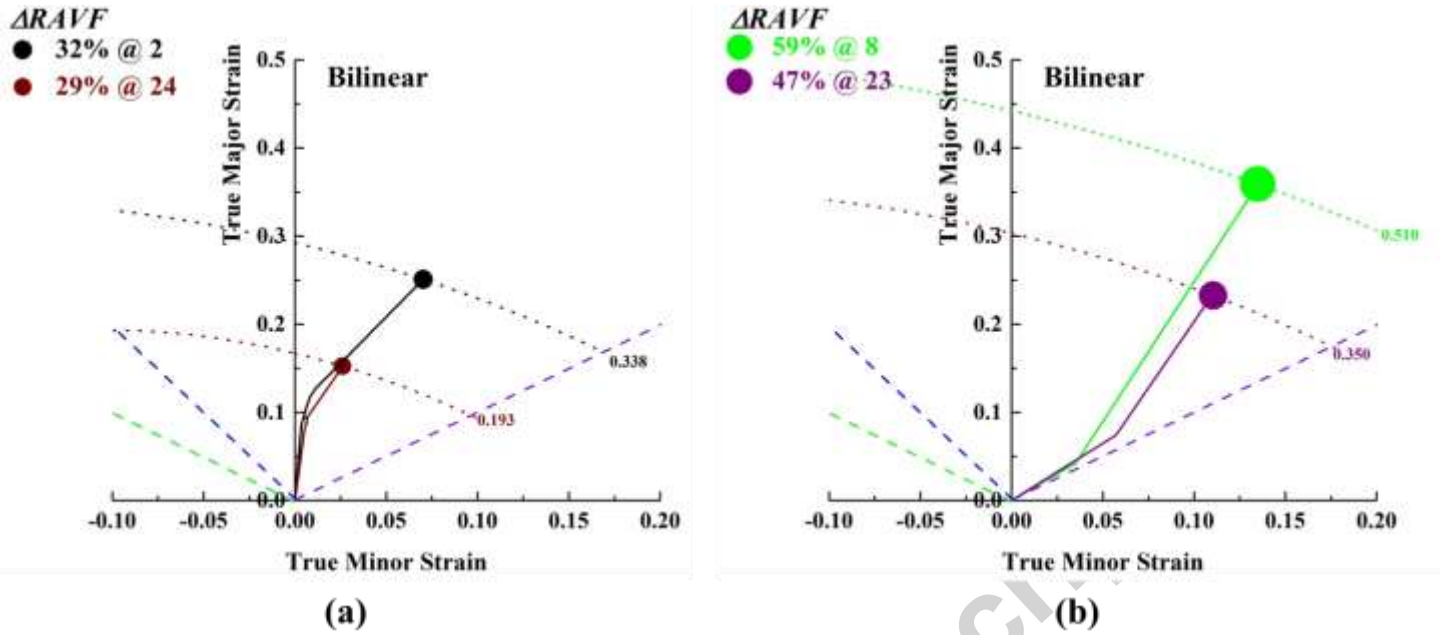

Figure 12 (a) and (b) The ε_{eff} level effect on $\Delta RAVF$ [see Eq. (3)] under different bilinear strain paths. The dashed (straight) lines denote shear (green), uniaxial tension (blue), and equibiaxial tension (purple) deformation modes. Dotted (curved) lines denote calculated ε_{eff} [see Eq. (2)] levels using DIC-measured true strains. Each is associated with a specific $\Delta RAVF$.

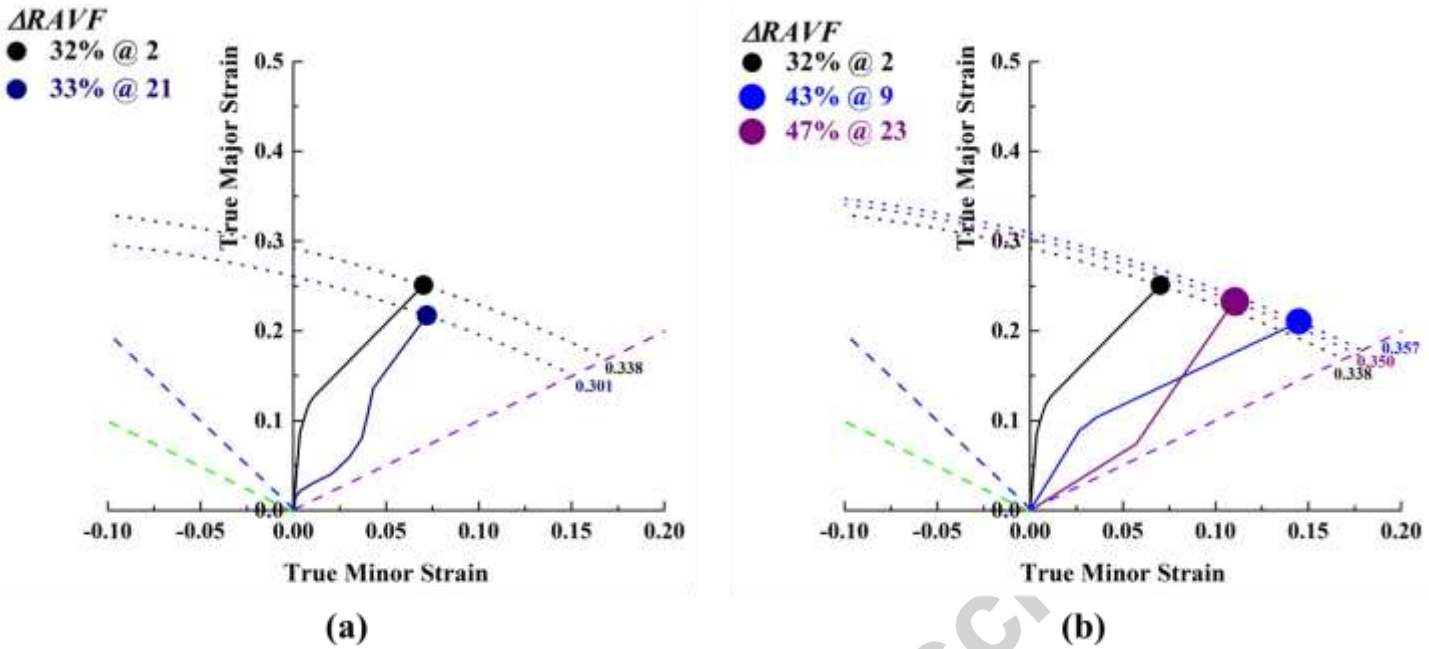

Figure 13 (a) and (b) The strain path effect on $\Delta RAVF$ [see Eq. (3)]. The dashed (straight) lines denote shear (green), uniaxial tension (blue), and equibiaxial tension (purple) deformation modes. Dotted (curved) lines denote calculated ε_{eff} [see Eq. (2)] levels using DIC-measured true strains. Each is associated with a specific $\Delta RAVF$.